

Extremely Large and Angle-Dependent Magnetoresistance in Kagome Dirac Semimetal RFe_6Sn_6 ($\text{R}=\text{Ho}, \text{Dy}$)

Susanta Ghosh^{a,c}, Achintya Low^{a,c}, Nayana Devaraj^b, Susmita Changdar^a, Awadhesh Narayan^b and Setti Thirupathaiah^{a,*}

^aS. N. Bose National Centre for Basic Sciences, Salt Lake, JD Block, Sector III, Bidhannagar, Kolkata, 700106, West Bengal, India

^bSolid State and Structural Chemistry Unit, Indian Institute of Science, Bangalore, 560012, Karnataka, India

^cThese authors contributed equally

ARTICLE INFO

Keywords:

Dirac Semimetal
Magnetic Materials
Magnetoresistance
Topological Hall effect
Angle-dependent Magnetoresistance

ABSTRACT

We report on the electronic, magnetic, and magneto-transport properties of Fe-based kagome Dirac system, RFe_6Sn_6 ($\text{R} = \text{Ho}, \text{Dy}$). Magnetic properties study reveals an antiferromagnetic order with Néel temperature of $T_N \approx 570$ K. Additionally, a weak ferromagnetic order emerge at low temperatures. Magnetotransport measurements demonstrate an extremely large magnetoresistance (XMR) reaching as high as $3 \times 10^3\%$ for HoFe_6Sn_6 and $1 \times 10^3\%$ for DyFe_6Sn_6 when measured at 2 K with 9 T of magnetic field. The semi-classical two-band model fitting of the Hall conductivity reveals nearly perfect electron-hole compensation and high carrier mobility, which leads to XMR behaviour in these system. Further, we identify large magnetoresistance anisotropy for the magnetic fields applied in different crystallographic orientations. In addition, considerable modification in the angle-dependent magnetoresistance (ADMR) pattern has been noticed between 2 and 50 K, indicating temperature-dependent changes in the Fermi surface topology of these systems.

1. Introduction

Magnetoresistance (MR) is the change in the longitudinal electrical resistivity under an external magnetic field (H), which is defined as $MR = [\rho(H) - \rho(0)]/\rho(0)$. Here, $\rho(H)$ and $\rho(0)$ are the resistivity measured with and without magnetic field, respectively. Extremely large MR in magnetic materials is a rare phenomena [1–3] but has potential technological applications in spintronics [4–6]. Therefore, searching for systems with extremely large magnetoresistance is a key research focus for physicists and materials scientists. Conventional non-magnetic metals generally display positive magnetoresistance (MR) [3, 7, 8], while ferromagnetic materials tend to exhibit negative MR [1, 3, 8]. In most of the bulk magnetic systems, the MR (%) values are relatively smaller and are typically below 5 % [1, 8, 9], while the giant magnetoresistance (GMR) is found in low dimensional systems such as in thin films or multilayered structures [3, 10]. Also, the colossal magnetoresistance (CMR) is mostly observed in the manganese-based perovskite oxides [3, 4]. On the other hand, the tunneling magnetoresistance (TMR) is observed in magnetic tunnel junctions (MTJs) produced by sandwiching a thin insulating barrier between two ferromagnetic layers [11]. Recently, an extremely large MR (XMR) of the order of $10^3\% - 10^8\%$ has been found in many nonmagnetic topological materials [12–17], triggering a great deal of research attention in this direction.


Though several topological systems have demonstrated the XMR in their bulk phase [13–16], in the topological kagome systems it is very rarely observed. To the best of our knowledge, $\text{Ni}_3\text{In}_2\text{S}_2$ is the only kagome system that


has been recently reported for the XMR behaviour [18]. The kagome lattice, made up of geometrically frustrated corner-sharing triangles, has gained much attention recently due to their distinctive characteristics, including the van Hove singularities, flat bands, and Dirac points in the electronic band structure. Numerous kagome materials have been found to exhibit several interesting physical properties. For instance, the Co-based kagome system $\text{Co}_3\text{Sn}_2\text{S}_2$ shows giant anomalous Hall effect (AHE), Chiral anomaly, and Weyl fermions [19, 20]. Despite being an antiferromagnet, the Mn-based kagome system Mn_3X ($\text{X}=\text{Sn}, \text{Ge}$) shows surprisingly large anomalous Hall effect, anomalous Nernst effect (ANE), and Weyl fermions [21–26]. Whereas, the vanadium based kagome systems AV_3Sb_5 ($\text{A}=\text{K}, \text{Rb}, \text{Cs}$) show topological superconductivity [27, 28].

In this regard, the RM_6X_6 ($\text{R} = \text{rare earth}, \text{M} = \text{transition metals}, \text{X} = \text{Sn}, \text{Ge}$) family of kagome systems have become a hot research topic due to their intriguing combination of electronic and magnetic properties. Within the RM_6X_6 kagome family, the researchers have so far focused on exploring the electronic and magnetic properties of the manganese (Mn)-based RMn_6X_6 [29–36] and the vanadium (V)-based RV_6X_6 [37–40] subfamilies but not much on the iron (Fe)-based RFe_6Sn_6 kagome family of systems. The only experimental report available on the Fe-based YFe_6Sn_6 system suggests a low magnetoresistance (MR) [41]. Therefore, in this manuscript we systematically studied the magnetic and magnetotransport properties of the Fe-based RFe_6Sn_6 ($\text{R} = \text{Ho}, \text{Dy}$) kagome systems.

2. Experimental and Computational details

Single crystals of RFe_6Sn_6 ($\text{R} = \text{Ho}, \text{Dy}$) were grown with Sn as flux using the high temperature muffle-furnace.

 setti@bose.res.in (S. Thirupathaiah)

 www.qmat.in (S. Thirupathaiah)

ORCID(S): 0000-0003-1258-0981 (S. Thirupathaiah)

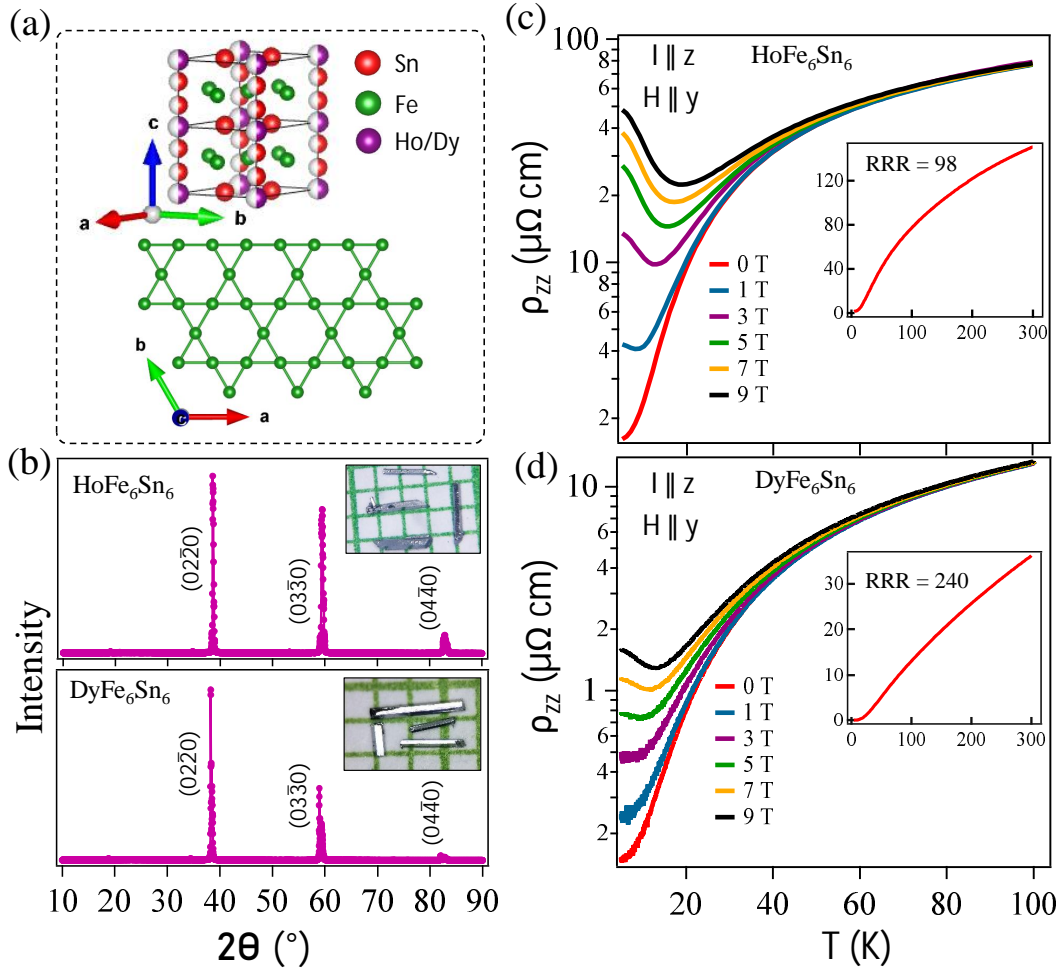


Figure 1: (a) Schematics of $R\text{Fe}_6\text{Sn}_6$ crystal structure. (b) Powder X-ray diffraction patterns taken on the single crystal of HoFe_6Sn_6 and DyFe_6Sn_6 . Insets in (b) show the photographic image of HoFe_6Sn_6 and DyFe_6Sn_6 single crystal. Temperature dependence of longitudinal resistivity (ρ_{zz}), measured at different transverse magnetic fields ($H \parallel y$) for HoFe_6Sn_6 (c) and DyFe_6Sn_6 (d). Inset of (c) and (d) show the temperature dependence of resistivity measured without magnetic field for HoFe_6Sn_6 and DyFe_6Sn_6 , respectively.

The starting elements of high purity R (Ho, Dy) ingot (99.9%, Alfa Aesar), Fe powder (99.99%, Stren Chemical), and Sn shorts (99.995%, Alfa Aesar) were mixed in the molar ratio of 1 : 6 : 30. Next, an evacuated quartz ampoule was used to seal the alumina crucible containing the mixture. The ampoule was then heated to 1000°C at a rate of 100°C/hr and held there for 18 hours, and cooled the molten mixture down to 600°C at a rate of 5°C/hr . After annealing for another five days at 600°C , the ampoule was promptly transferred to a centrifuge to separate the as-grown single crystals from Sn-flux. In this approach, we obtained many hexagonal rod-shaped $R\text{Fe}_6\text{Sn}_6$ ($R = \text{Ho, Dy}$) single crystals with a typical size of $(2 \times 0.3 \times 0.2) \text{ mm}^3$ as depicted in the inset of Fig. 1(b).

The phase purity and crystal structure of the as-grown single crystals were analyzed using the powder X-ray diffraction (XRD, 9 KW, Rigaku Smart Lab) and single crystal XRD (SXRD, SuperNova, Rigaku) techniques with Cu-K_α radiation ($\lambda = 1.5406 \text{ \AA}$). The elemental composition of

the as-grown single crystals were identified using energy-dispersive X-ray analysis (EDAX) coupled with scanning electron microscope (SEM, Quanta 250 FEG). The exact chemical composition were found to be the as-grown samples are found to be $\text{Ho}_{0.85}\text{Fe}_{6.12}\text{Sn}_{6.04}$ and $\text{Dy}_{1.16}\text{Fe}_{5.82}\text{Sn}_6$ using EDAX. For simplicity, we shall denote them by their nominal compositions of HoFe_6Sn_6 and DyFe_6Sn_6 , wherever applicable. Electrical transport, Hall effect, and magnetic properties were conducted using a 9 Tesla physical property measurement system (PPMS, Dynacool, Quantum Design) within the temperature range of 2-300 K. High temperature magnetic measurements up to 750 K were carried out using the VSM-oven option in the PPMS. Electrical transport and Hall effect properties were measured using the four-probe technique. For this, silver epoxy (EPO-TEK H20E) was used to attach copper leads to the sample.

Density functional theory (DFT) calculations were conducted using the Quantum ESPRESSO package [42]. We

employed ultrasoft pseudopotentials and Perdew-Burke-Ernzerhof (PBE) functional within the generalized gradient approximation (GGA) [43]. The kinetic energy cutoff for the wavefunction was at 140 Ry. To determine the equilibrium lattice parameters of HoFe_6Sn_6 and DyFe_6Sn_6 , variable-cell relaxation calculations were executed with a k -grid of $6 \times 6 \times 4$. For the density of states (DOS) calculations, a denser $12 \times 12 \times 8$ k -grid was utilized. The convergence threshold for the self-consistent field was taken as 10^{-9} Ry.

3. Results and Discussions

Fig. 1(a) schematically shows the primitive unit cell of the hexagonal crystal structure of RFe_6Sn_6 (top) and the crystal structure projected onto the ab -plane (bottom). From Fig. 1(a), we can see the ab -plane kagome lattice formed solely by the Fe-atoms. The XRD patterns obtained on the rod-shaped single crystals of RFe_6Sn_6 are shown in Fig. 1(b), displaying the $(0\ 2\ \bar{2}\ 0)$ Bragg's reflections, implying that the c -axis is the crystal growth axis. We further measured powder XRD on the crushed single crystals of RFe_6Sn_6 and performed Rietveld refinement using the Fullprof software (see Fig. S1 in supplementary information). Rietveld refinement confirms that HoFe_6Sn_6 and DyFe_6Sn_6 crystallize into the hexagonal YCo_6Ge_6 -type structure with a space group of $P6/mmm$ (191). The refined lattice parameters are $a = b = 5.3542$ (5) Å, $c = 4.4493$ (4) Å, $\alpha = \beta = 90^\circ$, $\gamma = 120^\circ$ for HoFe_6Sn_6 and $a = b = 5.3549$ (5) Å, $c = 4.4518$ (4) Å, $\alpha = \beta = 90^\circ$, $\gamma = 120^\circ$ for DyFe_6Sn_6 . The hexagonal crystal structure is further confirmed by the single crystal XRD (SCXRD) (see Fig. S2 in the supplemental information).

Figs. 1(c) and 1(d) exhibit temperature-dependent longitudinal electrical resistivity (ρ_{zz}) of HoFe_6Sn_6 and DyFe_6Sn_6 , respectively, measured under various magnetic fields for $H \parallel y$ direction. Inset of Figs. 1(c) and 1(d) depict temperature-dependent longitudinal electrical resistivity with zero magnetic field from respective samples, demonstrating a metallic behaviour throughout the measured temperature range. The residual resistivity ratio [$RRR = \rho_{zz}(300\text{K})/\rho_{zz}(2\text{K})$] is about 98 for HoFe_6Sn_6 and 240 for DyFe_6Sn_6 , suggesting good quality of the studied single crystals. As can be seen from Figs. 1(c) and 1(d), the low temperature resistivity [ρ_{zz} (T)] increases significantly with increasing field, demonstrating a significant magnetoresistance (MR) in the low temperature region.

Next, to explore the magnetic properties, temperature dependent magnetization [$M(T)$] and isothermal magnetization [$M(H)$] at different temperatures are performed for $H \parallel z$ and $H \parallel y$ directions. The top panels of Fig. 2 show the magnetization data of HoFe_6Sn_6 , whereas the bottom panels show the magnetization data of DyFe_6Sn_6 . From high temperature magnetisation data, we observe an antiferromagnetic transition at around 570 K for both HoFe_6Sn_6 and DyFe_6Sn_6 single crystals [see inset in Figs. 2(a) and 2(b)]. The magnetisation increases sharply at low temperatures, as seen in Fig. 2(a) and Fig. 2(b), suggesting a ferromagnetic

type ordering at low temperatures. Using the first derivative of temperature-dependent magnetization data (not shown here), we identified the ferromagnetic ordering temperature of $T_C \approx 5.1$ K from HoFe_6Sn_6 and 8.5 K from DyFe_6Sn_6 .

Figs. 2(c) and 2(d) show the isothermal magnetization [$M(H)$], measured at various temperatures for $H \parallel y$ from HoFe_6Sn_6 and DyFe_6Sn_6 single crystals, respectively. The $M(H)$ curves at 2 K and 10 K exhibit a rapid increase in the low-field region, followed by a slower increase in the high-field region, without reaching saturation up to an applied field of 9 T. In agreement to the magnetization data which suggest ferromagnetic nature at low temperatures, we observe magnetic hysteresis for both systems when measured at 2 K [see the inset in Figs. 2(c) and 2(d)]. Thus, HoFe_6Sn_6 and DyFe_6Sn_6 show ferrimagnetic nature at low temperatures. However, $M(H)$ shows linear behaviour above 50 K due to melting of FM state and leaving behind the antiferromagnetic state alone.

Figs. 2(e) and 2(f) show $M(H)$ data measured at various temperatures for $H \parallel z$ on HoFe_6Sn_6 and DyFe_6Sn_6 single crystals, respectively. Interestingly, the $M(H)$ data measured at 2 K shows a *kink* at around 5.25 T for HoFe_6Sn_6 and 6.33 T for DyFe_6Sn_6 , persisting up to 10 K [see Fig. S8 in Supplemental information], which indicates a field-induced metamagnetic state for $H \parallel z$. However, the metamagnetic state disappears at when measured at around 20 K for both HoFe_6Sn_6 and DyFe_6Sn_6 . Such a low-temperature metamagnetic state was observed earlier too in systems like DyV_6Sn_6 , HoV_6Sn_6 , RMn_6Ge_6 ($R = \text{Tb} - \text{Lu}$), RAuGe ($R = \text{Dy}, \text{Ho}, \text{and Gd}$) [32, 44, 45]. The metamagnetic state is commonly found in the rare-earth kagome based systems as the rare-earth ions such as Ho^{3+} or Dy^{3+} (in the present study) possess large, localized $4f$ magnetic moments that couple strongly to the crystalline electric field (CEF), giving rise to a pronounced single-ion magnetic anisotropy [45]. The anisotropy constrains the spins to align along the preferred crystallographic directions. Further, when the magnetic field is applied along the hard axis of magnetization, the interplay between the magnetic anisotropy and the exchange interactions induces sudden spin flip/flop or canted spin magnetic moments, leading to the metamagnetic state at a suitable temperature and magnetic field. In contrast to the $M(H)$ data measured for $H \parallel y$, magnetic hysteresis is not found from both HoFe_6Sn_6 and DyFe_6Sn_6 for $H \parallel z$. Nevertheless, similar to $H \parallel y$, the systems become completely antiferromagnetic above 50 K for $H \parallel z$ as well.

Earlier, in the case of Fe-based RFe_6Ge_6 and RFe_6Sn_6 ($R = \text{rare earth}$) series of intermetallic compounds an independent magnetic behaviour of the rare-earth (R) and Fe sublattices was identified [46–48]. In RFe_6Sn_6 , while the Fe sublattice shows an antiferromagnetic ordering below the Néel temperature of $T_N \approx 560$ K, the rare-earth sublattice orders ferromagnetically at significantly lower temperatures. For $R = \text{Gd} - \text{Er}$, the ferromagnetic ordering temperature of rare-earth sublattice ranges from 3 K for ErFe_6Ge_6 to 45 K for GdFe_6Sn_6 , without affecting the Fe sublattice AFM ordering temperature. Our experimental findings also

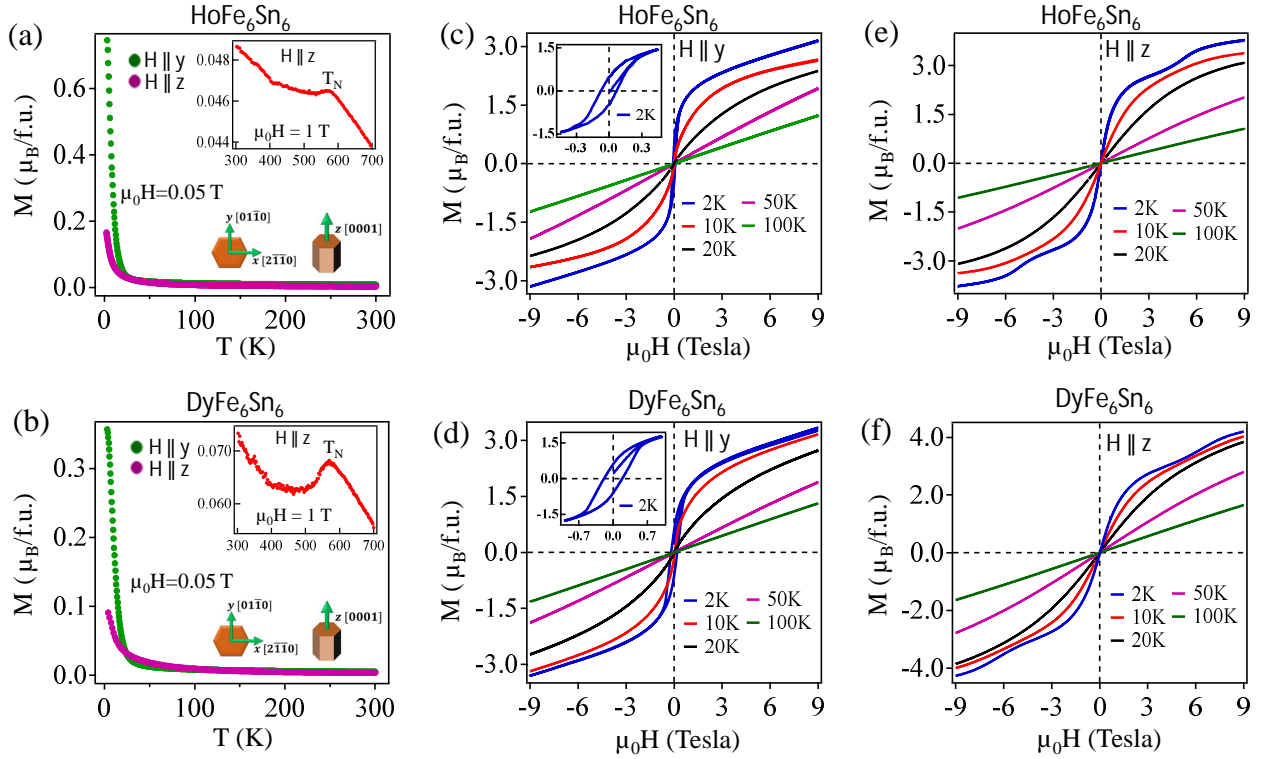


Figure 2: Temperature dependent magnetization [$M(T)$], measured for both $H \parallel z$ and $H \parallel y$ on the single crystals of (a) HoFe_6Sn_6 and (b) DyFe_6Sn_6 . The inset of (a) and (b) shows the high temperature $M(T)$ data of HoFe_6Sn_6 and DyFe_6Sn_6 , respectively. (c) and (d) show the magnetization isotherms [$M(H)$] measured at different temperatures for $H \parallel y$ from HoFe_6Sn_6 and DyFe_6Sn_6 , respectively. The inset of (c) and (d) shows the zoomed-in $M(H)$ at 2 K of HoFe_6Sn_6 and DyFe_6Sn_6 , respectively. Similarly, (e) and (f) show $M(H)$ data, measured at different temperatures for $H \parallel z$ from HoFe_6Sn_6 and DyFe_6Sn_6 , respectively.

reveal a similar magnetic ordering pattern for the HoFe_6Sn_6 and DyFe_6Sn_6 exhibiting an antiferromagnetic ordering at around 570 K whereas a ferromagnetic ordering is found at 5.1 K for HoFe_6Sn_6 and 8.5 K for DyFe_6Sn_6 . These observations are in well agreement with previous reports on similar systems [46–48]. Further, the estimated magnetic moment per Ho in HoFe_6Sn_6 is about $3.78 \mu_B$ for $H \parallel z$ and $3.11 \mu_B$ for $H \parallel y$. These values are substantially lower than the magnetic moments of free Ho^{3+} ($10.0 \mu_B$) ion. The same has been noticed from DyFe_6Sn_6 , that the magnetic moment per Dy is about $4.20 \mu_B$ for $H \parallel z$ and $3.34 \mu_B$ for $H \parallel y$, which is also substantially lower than the magnetic moment of free Dy^{3+} ($10.6 \mu_B$) ion. This observation clearly confirms that the magnetic moment of the measured systems is not fully polarised even at an external magnetic field of 9 T, resulting into the coexistence of both FM and AFM states in $\text{Ho}(\text{Dy})\text{Fe}_6\text{Sn}_6$ single crystals at low temperatures.

Next, coming to the important observations of this study, Figs. 3(a) and 3(b) depict the transverse magnetoresistance (MR), i.e., the resistance measured under transverse electric and magnetic fields, at different sample temperatures for HoFe_6Sn_6 and DyFe_6Sn_6 , respectively. Here, we measure MR with the current applied along z-axis and field applied along y-axis. We calculate MR using the relation $MR(\%) =$

$[\rho_{zz}(T, \mu_0 H) - \rho_{zz}(T, 0)] / \rho_{zz}(T, 0) \times 100\%$. In both systems, a positive non-saturating magnetoresistance was observed at all measured temperatures with the field applied up to 9 T. At 2 K and 9 T, MR reaches a maximum value of $3 \times 10^3\%$ for HoFe_6Sn_6 and $1 \times 10^3\%$ for DyFe_6Sn_6 . The value of MR decreases rapidly with increasing temperature and reaches 1% for HoFe_6Sn_6 and 2% for DyFe_6Sn_6 at 100 K and 9 T. This is surprising as the magnetic bulk intermetallic systems usually do not show large MR. Also, let us emphasize here that this is first study showing such as extremely large magnetoresistance from the magnetic Fe-based kagome systems. The only other kagome system reported to exhibit XMR is $\text{M}_3\text{In}_2\text{S}_2$ ($\text{M} = \text{Ni, Co}$) kagome systems [18, 49].

To understand the nature magnetoresistance, we fitted the field dependent MR with equation, $MR \propto B^m$ [see Fig. S3 in the supplementary information] [50]. From the fittings, we estimate $m \simeq 1.02$ for HoFe_6Sn_6 and 1.45 for DyFe_6Sn_6 at 2 K. At, 15 and 20 K, the MR follows linear field dependence ($m = 1$) for both crystals as shown in the inset of Figs. 3(a) and 3(b). At 100 K, we estimated $m \simeq 1.74$ for HoFe_6Sn_6 and 1.79 for DyFe_6Sn_6 [see Fig. S3 in the supplemental information]. Conventional MR generally changes quadratically with field, but in our case we find that the MR dependence on field changes with temperature. To further confirm this phenomenon, we performed scaling

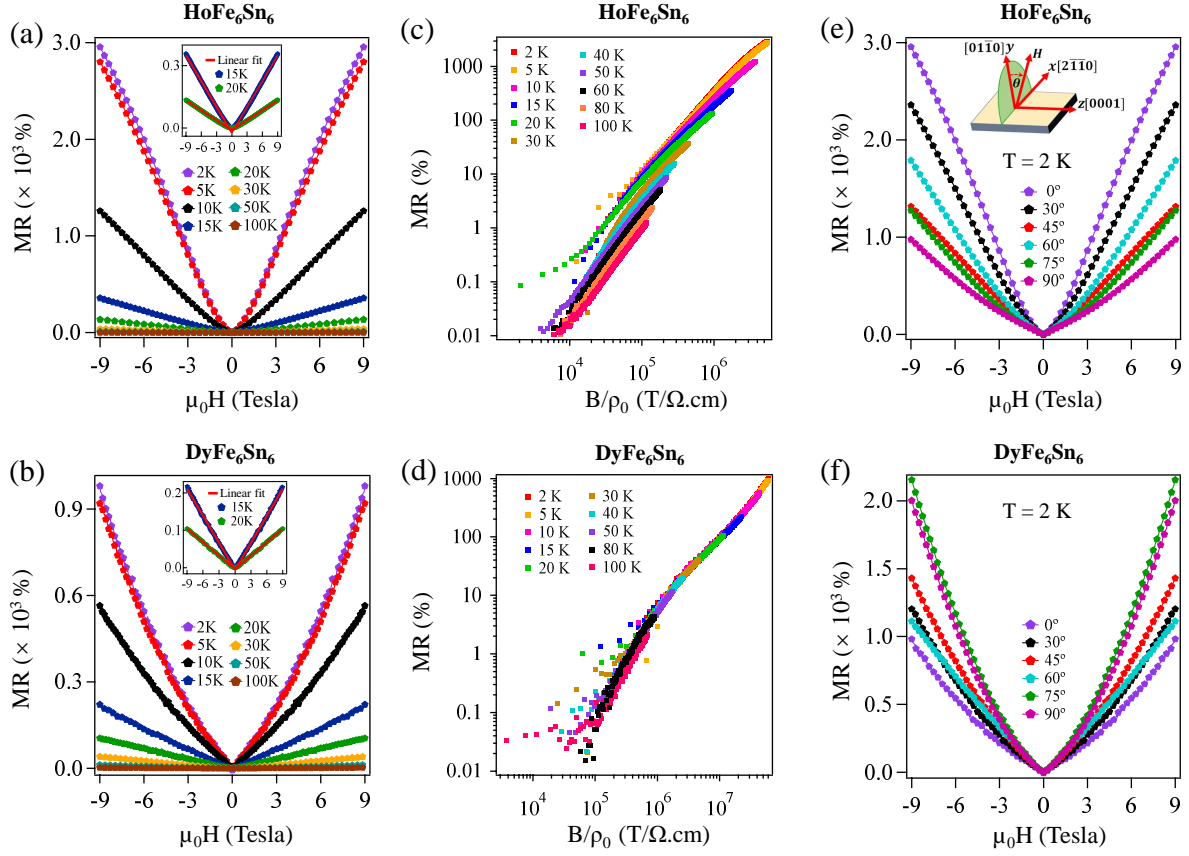


Figure 3: Magnetoresistance (MR) as a function of magnetic field is plotted for different temperatures from (a) HoFe_6Sn_6 and (b) DyFe_6Sn_6 . The insets of (a) and (b) show MR data taken 15 and 20 K MR overlapped with linear fit from HoFe_6Sn_6 and DyFe_6Sn_6 , respectively. Scaling analysis of MR data using Kohler's rule for various temperatures from (c) HoFe_6Sn_6 and (d) DyFe_6Sn_6 . MR as a function of field is measured at different field angles (θ) when rotated in the xy -plane from (e) HoFe_6Sn_6 and (f) DyFe_6Sn_6 . The inset in (e) illustrates measurement geometry.

analysis using the Kohler's rule and plotted the MR curves as a function of B/ρ_0 (Kohler's plot) measured at different temperatures as shown in Figs. 3(c) and 3(d). From the Kohler's plots it is evident that the MR curves do not collapse onto a single universal curve for all measured temperatures, indicating the break down of Kohler's rule. The violation of Kohler's rule suggests a single scattering mechanism is not applicable to explain the MR in the studied systems. Therefore, different temperature regions have distinct scattering mechanism [18, 51, 52].

Further, we measured the field-dependent MR at 2 K by applying the magnetic field along different crystallographic axis while fixing the current direction. The inset of Fig. 3(e) schematically shows the angle-dependent MR (ADMR) configuration, with the current along the z [0001] axis and the magnetic field direction varies in the xy -plane. As can be seen from Fig. 3(e), in HoFe_6Sn_6 , the MR gradually decreases from 3×10^3 % to 1×10^3 % as the angle θ increases from 0° to 90° . Conversely, the MR in DyFe_6Sn_6 increases from 1×10^3 % to 2×10^3 % as we increase θ from 0° to 90° and reaching maximum 2.2×10^3 at $\theta = 75^\circ$ [Fig. 3(f)]. Thus, we can see that the MR is highly crystallographic axis dependent. To further investigate the directional dependent

MR, we fit the data using a power law function ($\text{MR} \propto B^m$) at different angles as shown in the Fig. S4 of the supplemental information. From the fittings, we estimate $m \simeq 1.02$, 1 and 1.36 at the angles 0° , 45° and 90° for HoFe_6Sn_6 and 1.45, 1, and, 1.54 at the angles 0° , 60° and 90° for DyFe_6Sn_6 , respectively. We find linear MR at 15 and 20 K for both the HoFe_6Sn_6 and DyFe_6Sn_6 systems at an angle of 0° .

For more insights on the angle-dependent magnetoresistance (ADMR), we measured MR at different temperatures under a fixed magnetic field of 9 T and by rotating the field direction with respect to the crystal axis as shown in Figs. 4(a) and 4(b) for HoFe_6Sn_6 and DyFe_6Sn_6 , respectively. For a given field and temperature the ADMR is calculated using the formula, $\text{ADMR}(\%) = \frac{\rho_{zz}(\theta) - \rho_{zz}(\theta_{\min})}{\rho_{zz}(\theta_{\min})} \times 100\%$. θ_{\min} is about 86° for HoFe_6Sn_6 , whereas θ_{\min} is about 196° for DyFe_6Sn_6 . In Fig. 4(a), the ADMR measured at 2 K shows a total of 12 local maxima and 12 local minima, resulting in a total of 12 lobes for HoFe_6Sn_6 . This pattern remains unchanged up to 10 K. However, as the temperature increases further the ADMR pattern evolves by decreasing the number of lobes. Similarly, in Fig. 4(b), the ADMR at 2 K for DyFe_6Sn_6 displays 8 local maxima and 8 local

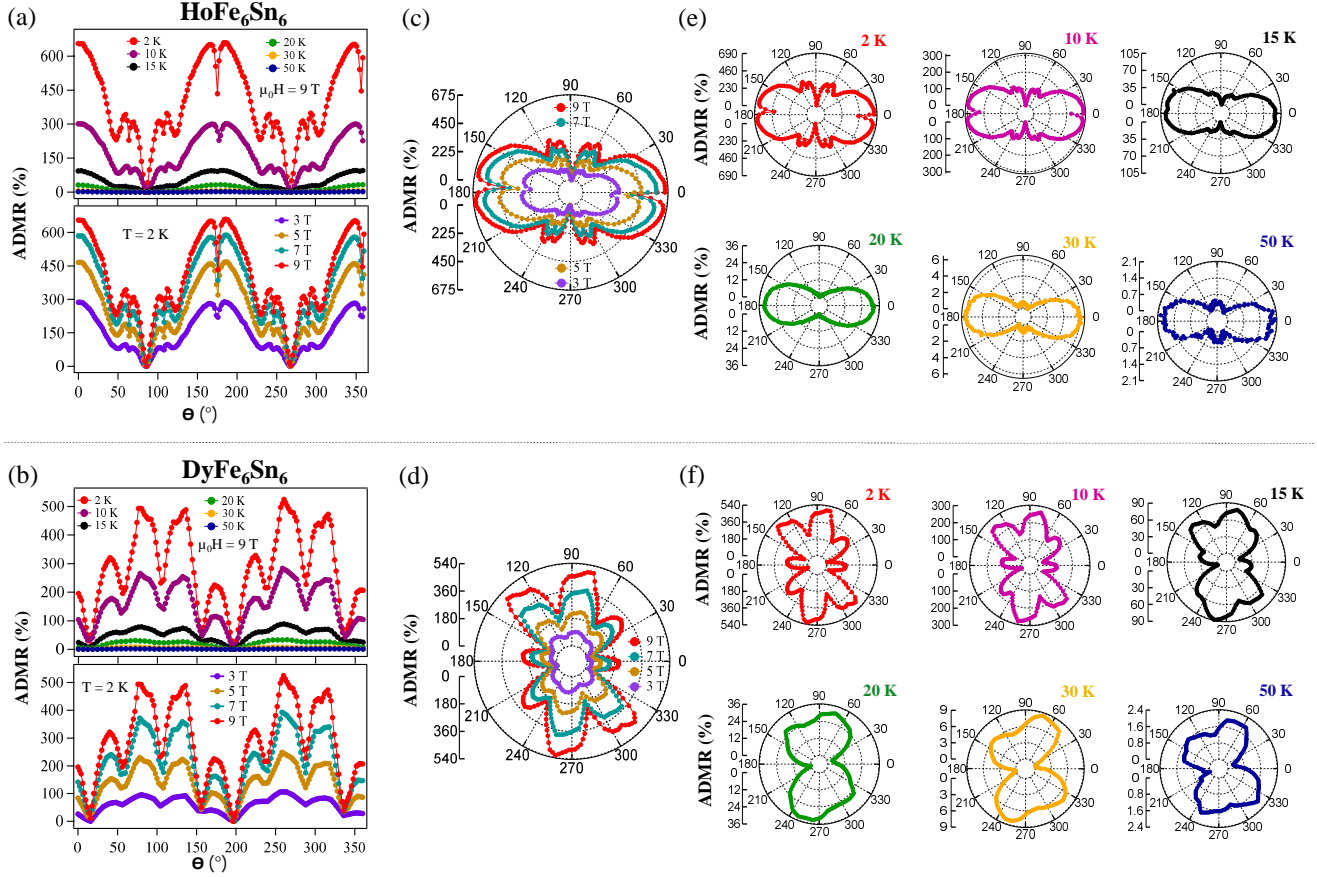


Figure 4: Angular-dependent magnetoresistance (ADMR) measured for (a) HoFe_6Sn_6 and (b) DyFe_6Sn_6 by varying the temperature at a fixed magnetic field of 9 T (top panels) and by varying the magnetic fields at a fixed temperature of 2 K (bottom panels). Current flows along the z -axis and the field is rotated within the xy -plane as depicted in the inset of Fig. 3(e). Polar plot of ADMR measured at 2 K by varying the field for (c) HoFe_6Sn_6 and (d) DyFe_6Sn_6 . Polar plot of ADMR measured at 9 T by varying the temperature for (e) HoFe_6Sn_6 and (f) DyFe_6Sn_6 .

minima, forming the ADMR pattern with 8 lobes. As the temperature increases, the number of lobes decreases similar to HoFe_6Sn_6 . From Figs. 4(a) and 4(b), it is evident that the MR is highly sensitive to field angle, indicating the presence of strong anisotropic MR in these systems.

For a better visualization, we plotted the ADMR in polar graphs as depicted in Figs. 4(c)-4(f). Figs. 4(c) and 4(d) show the polar-plot of ADMR measured at 2 K under different magnetic fields for HoFe_6Sn_6 and DyFe_6Sn_6 , respectively. Figs. 4(e) and 4(f) show the polar-plot of ADMR measured under an applied field of 9 T at various sample temperatures for HoFe_6Sn_6 and DyFe_6Sn_6 , respectively. Further, from Fig. 4(c), we can see a butterfly-like ADMR pattern for HoFe_6Sn_6 at 2 K and the pattern remains almost constant, though the value of MR% decreases with decreasing field. Similarly, ADMR pattern of DyFe_6Sn_6 [see Fig. 4(d)] also looks butterfly-like but rotated by 90° . On the other hand, from Figs. 4(e) and 4(f), one can clearly see that the polar-plot of ADMR changes significantly with temperature. Importantly, the evolution of ADMR with temperature is different between HoFe_6Sn_6 and DyFe_6Sn_6 . For instance, in the case of HoFe_6Sn_6 [see Fig. 4(e)], the butterfly-like pattern

with 12 lobes are visible at 2 and 10 K. As the temperature rises, the ADMR pattern changes from a butterfly-like to a dumbbell-like at 20 K, with only two lobes visible. Further increasing the temperature, at 30 and 50 K, an additional two lobes have reemerged at 90° and 180° . In the case of DyFe_6Sn_6 [see Fig. 4(f)], the butterfly pattern, with eight lobes, is visible up to 15 K. Between 20 and 50 K, only four lobes are visible.

Next, Figs. 5(a) and 5(b) depict the ADMR measured at 2 K under the magnetic field of 9 T for HoFe_6Sn_6 and DyFe_6Sn_6 , respectively. The ADMR data is fitted by Eq. 1 having contribution up to 8-fold symmetry. Although the fitting is not perfect, the Eq. 1 can reasonably reproduce the experimental data. The fittings for higher temperature ADMR data are shown in the Fig. S5 of the supplemental information. The normalized relative amplitudes C_2 (two-fold), C_4 (four-fold), C_6 (six-fold), and C_8 (eight-fold) of ADMR are plotted as a function of temperature in Figs. 5(c) and 5(d) for HoFe_6Sn_6 and DyFe_6Sn_6 , respectively. From the temperature dependent relative amplitudes, we can notice that all symmetry components contribute to the ADMR

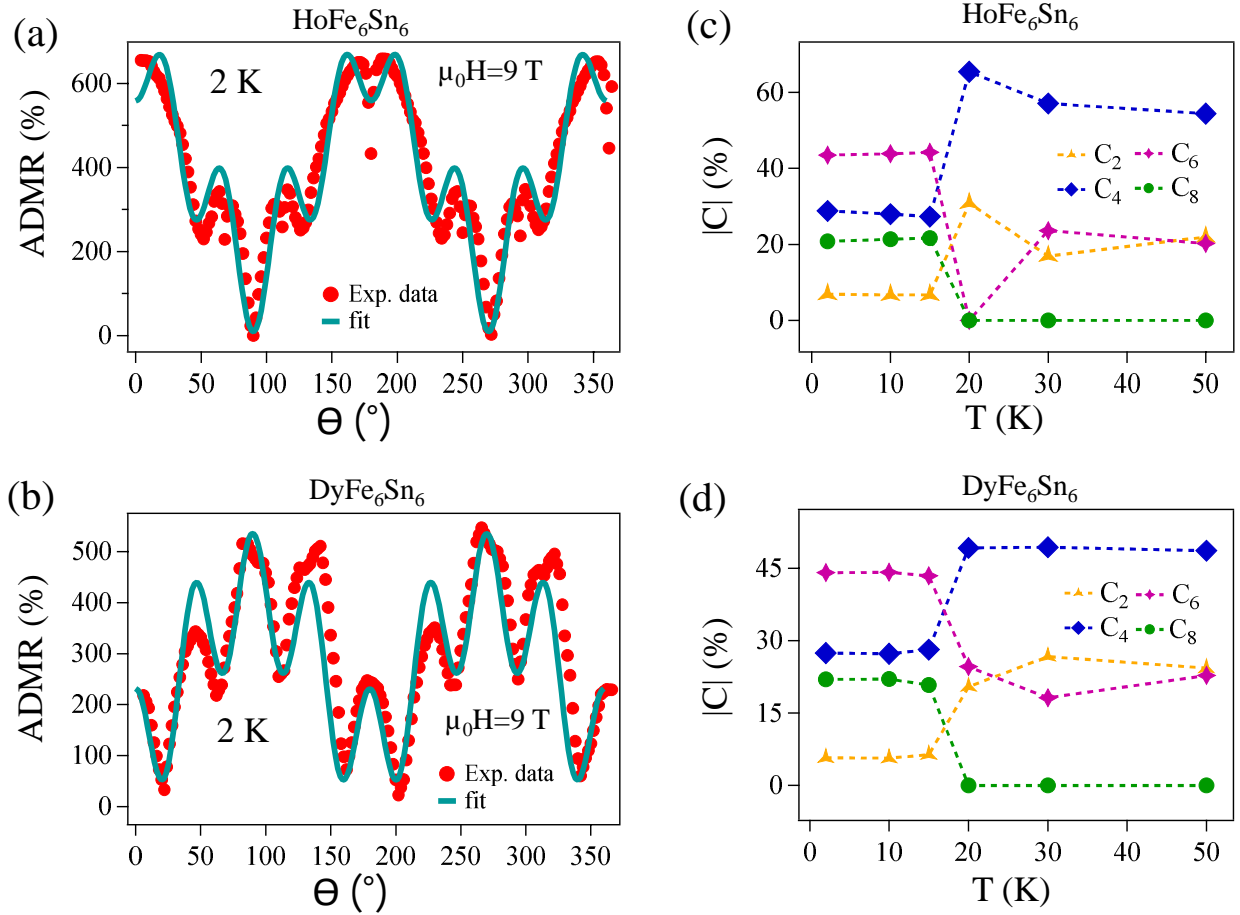


Figure 5: ADMR measured for (a) HoFe_6Sn_6 and (b) DyFe_6Sn_6 at 2 K and 9 T. The solid curves are fits of ADMR using the Eq. 1 (see the text for more details). The normalized relative amplitudes (absolute values) C_2 (two-fold), C_4 (four-fold), C_6 (six-fold), and C_8 (eight-fold) components of the ADMR as a function of temperature are shown for (c) HoFe_6Sn_6 and (d) DyFe_6Sn_6 . In (c) and (d), $|C_{2n}| = C_{2n} / \sum_{n=1}^4 C_{2n}$.

up to 20 K. However, from 20 K, the eight-fold symmetry contribution to ADMR is totally suppressed.

$$\text{ADMR} = C_0 + C_2 \cos^2 \theta + C_4 \cos^4 \theta + C_6 \cos^6 \theta + C_8 \cos^8 \theta \quad (1)$$

where C_0 is a constant, $C_2 \cos^2 \theta$, $C_4 \cos^4 \theta$, $C_6 \cos^6 \theta$, and $C_8 \cos^8 \theta$ account for the two, four, six, and eight fold components, respectively. The constants C_2 , C_4 , C_6 , and C_8 are the amplitudes.

Several mechanisms exist in the literature explaining the manifold symmetric ADMR, such as (i) magnetocrystalline anisotropy [53–55], (ii) spin scattering near the antiphase boundaries (APBs) [56–58], (iii) exchange bias [59], (iv) relaxation time anisotropy [49, 60], (v) valleytronics [61], (vi) symmetry of the lattice [49, 62], or (vii) density of states modulation near the Fermi level (such as Lifshitz transitions) [60, 63]. As can be seen from Figs. 4(c) and 4(d), the ADMR is insensitive to the applied field. Therefore, the observed ADMR in HoFe_6Sn_6 and DyFe_6Sn_6 may not be originated from the magnetism. Further, the mean

free path of the charge carriers calculated from Hall effect measurement data (shown later) at 2 K is about $25.20 \mu\text{m}$ for HoFe_6Sn_6 and $15.96 \mu\text{m}$ for DyFe_6Sn_6 , which are much higher than the distance of $\text{Fe} - \text{Fe}$ (2.67 Å), $\text{Ho} - \text{Ho}$ (5.35 Å), or $\text{Dy} - \text{Dy}$ (5.35 Å) magnetic moments. Therefore, we can neglect the spin-charge scattering in these systems, allowing us to safely exclude the influence of magnetism on the observed ADMR as discussed in the points (i)–(iv). Also, we can safely neglect the valleytronic origin of ADMR as the valleys are highly sensitive to the orientation and magnitude of the applied magnetic field [64] which is not the case in the current study. The other possibilities of ADMR are the crystal symmetry or the band structure near the Fermi level. As discussed above, the studied systems shows 2-, 4-, 6-, and 8-fold symmetry in the ADMR at low temperature (< 20 K) and at higher temperatures the 8-fold component completely gets suppressed leaving only the 2-, 4-, and 6-fold symmetries. Particularly, the 2-fold symmetry contribution is very small at low temperatures, and thus the total ADMR is dominated by the higher-fold symmetries. At higher temperatures, except the 8-fold symmetry component, the other symmetries significantly contribute to the

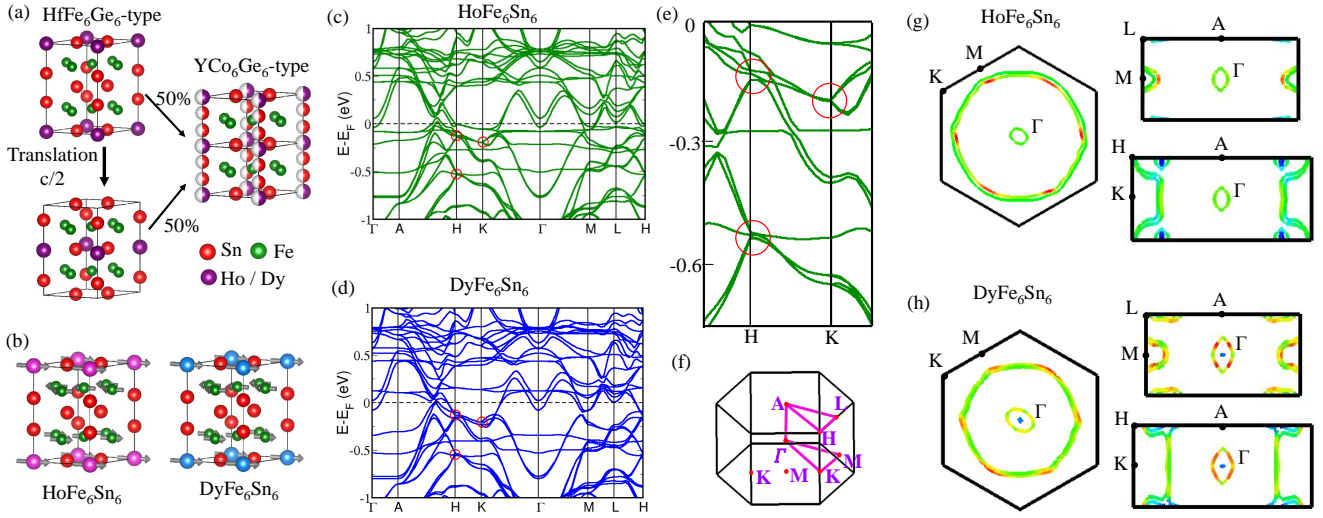


Figure 6: (a) Schematic demonstration of two HfFe₆Ge₆-type crystal structures forming one partially filled YCo₆Ge₆. (b) Ground state magnetic structure of HoFe₆Sn₆ and DyFe₆Sn₆, derived from the DFT calculations. (c) and (d) Electronic band structures of HoFe₆Sn₆ and DyFe₆Sn₆, respectively, calculated without including spin-orbit coupling (SOC). (e) Zoomed-in image of the (c) highlighting the Dirac-like band dispersions near the Fermi level. (f) Hexagonal Brillouin zone with high symmetry points located. (g) and (h) In-plane and out-of-plane Fermi contours of HoFe₆Sn₆ and DyFe₆Sn₆, respectively, calculated without including SOC.

total ADMR. Since the field is applied always perpendicular to the z -axis and is rotated within the xy -plane, the 6-fold symmetry contribution could be originated from the DOS modulation near the Fermi level and from the hexagonal crystal symmetry. On the other hand, the 2-fold and 4-fold symmetry contributions to the ADMR might have originated from the DOS modulation near the Fermi level [49, 60, 63]. This is because, in the momentum space, the charge carriers orbit around the Fermi surface cross-sections that are perpendicular to the magnetic field (B) direction [65]. As a result, the anisotropic shape of the Fermi surface leads to variation in the cyclotron mass and velocity, following the relation $v_k = \frac{1}{\hbar} \nabla_k \epsilon_k$. This variation in the cyclotron mass and velocity, has an effect on how easily the charge carrier trajectories bend under the magnetic field, influence the value of MR [65, 66].

To better understand band structure contribution to the anisotropic MR in these systems, we performed the density functional theory (DFT) calculations. Performing DFT calculations on Ho(Dy)Fe₆Sn₆ (YCo₆Ge₆-type structure) system is quite challenging due to its disordered nature. As illustrated in Fig. 6(a), the YCo₆Ge₆-type structure can be viewed as a combination of two HfFe₆Ge₆-type unit cells where one of them is translated by $c/2$ [41, 67]. To address the challenges associated with the disordered and partially occupied YCo₆Ge₆-type structure, we used the ordered HfFe₆Ge₆-type structure for the DFT calculations. This approach aligns well with previous studies on the related systems [41, 68]. Although the HfFe₆Ge₆-type and YCo₆Ge₆-type structures share the same space group ($P6/mmm$, 191), they differ in their atomic arrangement. Our DFT calculations suggest that in the ground state the Fe magnetic moments align antiferromagnetically, while the

Ho(Dy) magnetic moments align ferromagnetically within the ab -plane as shown in Fig. 6(b). This prediction is inline with our magnetization measurements which suggest that the easy magnetization axis lies on the ab -plane [see Fig. 2].

Figs. 6(c) and 6(d) show the electronic band structure plotted for HoFe₆Sn₆ and DyFe₆Sn₆, respectively, without considering the spin-orbit coupling (SOC). The band dispersions of both systems qualitatively look similar. Both band structures exhibit several parabolic bands crossing the Fermi level, confirming the metallic nature of the studied systems. Interestingly, we notice several non-dispersive flat bands near the Fermi level mostly contributed by the Ho(Dy) $4f$ orbitals [see Fig.S7 in the supplemental information] [37, 69, 70]. Further, from a zoomed-in band structure shown in Fig. 6(e), we observe several Dirac-like band crossings in the vicinity of the Fermi level marked by red-circles. These band crossings are mainly originating from the Fe $3d$ orbitals. Next, Figs. 6(g) and 6(h) show the Fermi maps of HoFe₆Sn₆ and DyFe₆Sn₆, respectively, from the in-plane and out-of-plane momentum space. From the in-plane (Γ -K-M) Fermi map, we mainly observe one small and two large Fermi sheets around Γ point. On comparing the Fermi sheets with the electronic band dispersions shown in Fig. 6(e), we can conclude that the two large Fermi contours are of hole-type and the smaller one is of electron-type.

Similarly, from the Fermi map taken in the Γ -M-L-A plane, we could observe two small electron-like highly dispersive out-of-plane Fermi sheets along the $M-L$ direction and another electron-type Fermi sheet dispersing along the $\Gamma-A$ direction. In addition, from the Fermi map taken in the Γ -K-H-A plane, we could observe two out-of-plane highly dispersive large electron-type Fermi sheets along the $K-H$ direction and two hole-like in-plane Fermi sheets along the

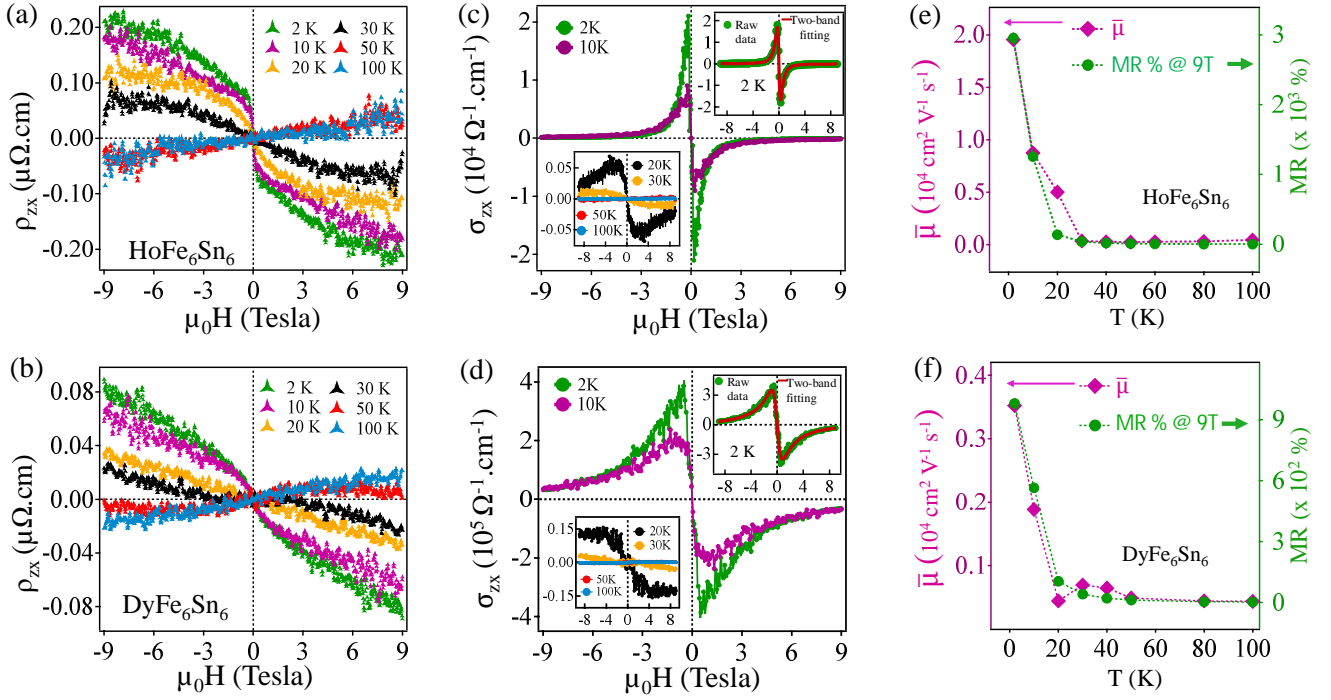


Figure 7: Field-dependent Hall resistivity (ρ_{zx}) measured at various temperatures for (a) HoFe_6Sn_6 and (b) DyFe_6Sn_6 . Hall conductivity (σ_{zx}) derived from Hall resistivity (ρ_{zx}) at 2 K and 10 K of (c) HoFe_6Sn_6 and (d) DyFe_6Sn_6 . Bottom left inset of (c) and (d) are the Hall conductivity (σ_{zx}) derived at 20 and 30 K. Top right inset of (c) and (d) show two-band model fitting of σ_{zx} at 2 K. Mean carrier mobility (left axis), $\bar{\mu} = \sqrt{\mu_h \mu_e}$ and MR(%) at 9 T (right axis) are plotted as a function of temperature for (e) HoFe_6Sn_6 and (f) DyFe_6Sn_6 .

$H - A$ direction. Since the applied field is perpendicular to the $z(k_z)$ -axis, the Fermi sheets lying in the ΓKHA and ΓMLA planes contribute to the magnetoresistance. And can be seen from Figs. 6(g) and 6(h), the Fermi sheets in these planes show 2- and 4-fold (nearly) symmetries. On rotating the magnetic field axis in the xy -plane, we could get the 6-fold modulation of the Fermi sheets of the ΓKHA and ΓMLA planes. We note that the band structures presented here are calculated without spin-orbit coupling. Spin-orbit coupling calculations are very challenging and lead to convergence issues due to the presence of $4f$ states.

Next, as the Hall effect is sensitive to the topological band structure, we performed Hall effect measurements for both HoFe_6Sn_6 and DyFe_6Sn_6 systems. The field-dependent Hall resistivity (ρ_{zx}) measured at different temperatures is shown in Figs. 7(a) and 7(b) for HoFe_6Sn_6 and DyFe_6Sn_6 , respectively. Here, ρ_{zx} corresponds to the current applied along the z -direction, field applied along the y -direction, and the Hall voltage was measured along the x -direction. From Fig. 7(a), it is clear that the Hall resistivity is not linear with magnetic field, suggesting more than one-type of charge carriers dominating the magnetotransport. Importantly, the slope of ρ_{zx} vs. H curve is positive below 30 K and negative for 50 and 100 K. We could not measure the Hall effect above 100 K due to high noise to signal ratio. Similar behaviour was also observed from DyFe_6Sn_6 as shown in Fig. 7(b). Figs. 7(c) and 7(d) show the Hall

conductivity (σ_{zx}) calculated from the Hall resistivity (ρ_{zx}) and longitudinal resistivity (ρ_{zz}) data using the equation,

$$\sigma_{zx} = -\frac{\rho_{zx}}{\rho_{zz}^2 + \rho_{zx}^2} \quad (2)$$

Following the semiclassical two band model, we fitted the Hall conductivity σ_{zx} using the equation,

$$\sigma_{zx} = \left[\frac{n_h \mu_h^2}{1 + (\mu_h B)^2} - \frac{n_e \mu_e^2}{1 + (\mu_e B)^2} \right] eB \quad (3)$$

where $n_h(n_e)$ and $\mu_h(\mu_e)$ are hole (electron) density and mobility, respectively. The two-band fitting of σ_{zx} at 2 K are shown in the top right inset of Fig. 7(c) and Fig. 7(d) for HoFe_6Sn_6 and DyFe_6Sn_6 , respectively. From the Hall conductivity fitting of HoFe_6Sn_6 at 2 K, the hole and electron density are found to be $n_h = 0.64 \times 10^{19} \text{ cm}^{-3}$ and $n_e = 0.69 \times 10^{19} \text{ cm}^{-3}$. The ratio of hole and electron density $n_h/n_e = 0.93$, which is close to 1 for a perfect electron-hole compensation. Also, the hole and electron mobility are found to be $\mu_h = 1.05 \times 10^4 \text{ cm}^2 \text{ V}^{-1} \text{ s}^{-1}$ and $\mu_e = 3.62 \times 10^4 \text{ cm}^2 \text{ V}^{-1} \text{ s}^{-1}$, respectively, for HoFe_6Sn_6 . The mean mobility is estimated to be $\bar{\mu} = 1.5 \times 10^4 \text{ cm}^2 \text{ V}^{-1} \text{ s}^{-1}$, using the relation $\bar{\mu} = \sqrt{\mu_h \mu_e}$ [12]. The mean mobility in this system is high and comparable to the numerous other systems showing XMR [3, 13, 71–73].

Further, in Fig. 7(e) we can notice that the mean carrier mobility rapidly decreases with increasing temperature between 2 and 100 K. Additionally, we also notice that the MR% value drops between 2 and 100 K in a similar fashion of the mean mobility [see Fig. 7(e)]. This observation suggests that the carrier mobility has a significant influence on the observed XMR and ADMR [see Fig. 5]. According to the earlier reports, XMR behaviour in $\alpha - WP_2$ strongly depends on the high carrier mobility rather than electron-hole compensation, which is consistent with our observation in HoFe_6Sn_6 [74]. Note that the band dispersions near the Fermi level controls the carrier mobility, and thus it is the electronic band structure playing the dominant role of ADMR in these systems. Further, DyFe_6Sn_6 also exhibits similar behaviour of carrier mobility to that of HoFe_6Sn_6 . In DyFe_6Sn_6 at 2 K, the hole and electron density are found to be $n_h = 3.95 \times 10^{20} \text{ cm}^{-3}$ and $n_e = 3.77 \times 10^{20} \text{ cm}^{-3}$, respectively. The ratio of hole and electron density is $n_h/n_e = 1.05$. The hole and electron mobility are found to be $\mu_h = 0.10 \times 10^4 \text{ cm}^2 \text{ V}^{-1} \text{ s}^{-1}$ and $\mu_e = 1.18 \times 10^4 \text{ cm}^2 \text{ V}^{-1} \text{ s}^{-1}$, yielding the mean mobility of $\bar{\mu} = 0.35 \times 10^4 \text{ cm}^2 \text{ V}^{-1} \text{ s}^{-1}$.

4. Summary

In conclusion, we systematically studied the magnetic and magnetotransport properties on the high-quality single crystals of the Fe-based RFe_6Sn_6 ($\text{R} = \text{Ho}, \text{Dy}$) kagome systems. Extremely large magnetoresistance (XMR) is observed at low temperatures reaching the maximum MR percentage as high as $3 \times 10^3 \%$ for HoFe_6Sn_6 and $1 \times 10^3 \%$ for DyFe_6Sn_6 at 2 K under 9 T of applied magnetic field. Hall effect measurements demonstrate the electron-hole charge compensation and high-carrier mobility, leading to extremely large magnetoresistance at low temperatures. Further, the angle-dependent magnetoresistance (ADMR) data reveal high anisotropy in the magnetoresistance. Importantly, the magnetoresistance anisotropic pattern changes significantly with temperature, implies the temperature dependence of the Fermi surface topology in these systems.

5. Acknowledgement

N.D. acknowledges IoE-IISc Postdoctoral Fellowship. S.G. acknowledges the University Grants Commission (UGC), India for the Ph.D. fellowship. A.N. acknowledges support from DST Nano Mission (project no. DST/NM/TUE/QM-10/2019(G)/1). S.T. thanks Anusandhan National Research Foundation (ANRF), India, through Grant no. CRG/2023/000748. S.T. thanks SERB (DST), India for the financial support through Grant no. SRG/2020/00393. The experimental work conducted in this research utilized the Technical Research Centre (TRC) Instrument Facilities at S. N. Bose National Centre for Basic Sciences, established as part of the TRC project funded by the Department of Science and Technology, Government of India.

References

- [1] C. W. Heaps, The Magnetoresistance of Nickel in Large Fields, *Physical Review* 55 (1939) 1069–1071.
- [2] S. S. P. Parkin, N. More, K. P. Roche, Oscillations in exchange coupling and magnetoresistance in metallic superlattice structures: Co/Ru, Co/Cr, and Fe/Cr, *Phys. Rev. Lett.* 64 (1990) 2304–2307.
- [3] R. Niu, W. Zhu, Materials and possible mechanisms of extremely large magnetoresistance: a review, *J. Phys. Condens. Matter* 34 (2021) 113001.
- [4] A. P. Ramirez, Colossal magnetoresistance, *J. Phys. Condens. Matter* 9 (1997) 8171–8199.
- [5] S. Yang, J. Zhang, Current progress of magnetoresistance sensors, *Chemosensors* 9 (2021) 211.
- [6] O. Vitayaya, P. Z. Z. Nehan, D. R. Munazat, M. T. E. Manawan, B. Kurniawan, Magnetoresistance (MR) properties of magnetic materials, *RSC Advances* 14 (2024) 18617–18645.
- [7] A. B. Pippard, Magnetoresistance in metals, volume 2, Cambridge university press, 1989.
- [8] S. Blundell, Magnetism in condensed matter, OUP Oxford, 2001.
- [9] J. Nickel, Magnetoresistance overview, Hewlett-Packard Laboratories, Technical Publications Department Palo Alto ..., 1995.
- [10] E. Tsymlal, D. Pettifor, Perspectives of giant magnetoresistance, 2001. URL: [https://doi.org/10.1016/S0081-1947\(01\)80019-9](https://doi.org/10.1016/S0081-1947(01)80019-9). doi:10.1016/S0081-1947(01)80019-9.
- [11] J. Inoue, S. Maekawa, Theory of tunneling magnetoresistance in granular magnetic films, *Phys. Rev. B* 53 (1996) R11927–R11929.
- [12] M. N. Ali, J. Xiong, S. Flynn, J. Tao, Q. Gibson, L. M. Schoop, T. Liang, N. Haldolaarachchige, M. Hirschberger, N. P. Ong, R. J. Cava, Large, non-saturating magnetoresistance in WTe_2 , *Nature* 514 (2014) 205–208.
- [13] F. Han, J. Xu, A. S. Botana, Z. L. Xiao, Y. L. Wang, W. G. Yang, D. Y. Chung, M. G. Kanatzidis, M. R. Norman, G. W. Crabtree, W. K. Kwok, Separation of electron and hole dynamics in the semimetal LaSb , *Phys. Rev. B* 96 (2017) 125112.
- [14] W. Gao, N. Hao, F.-W. Zheng, W. Ning, M. Wu, X. Zhu, G. Zheng, J. Zhang, J. Lu, H. Zhang, C. Xi, J. Yang, H. Du, P. Zhang, Y. Zhang, M. Tian, Extremely Large Magnetoresistance in a Topological Semimetal Candidate Pyrite PtBi_2 , *Phys. Rev. Lett.* 118 (2017) 256601.
- [15] K. Okawa, M. Kanou, H. Namiki, T. Sasagawa, Extremely large magnetoresistance induced by hidden three-dimensional Dirac bands in nonmagnetic semimetal InBi , *Phys. Rev. Mater.* 2 (2018) 124201.
- [16] C. Shekhar, A. K. Nayak, Y. Sun, M. Schmidt, M. Nicklas, I. Leermakers, U. Zeitler, Y. Skourski, J. Wosnitza, Z. Liu, Y. Chen, W. Schnelle, H. Borrmann, Y. Grin, C. Felser, B. Yan, Extremely large magnetoresistance and ultrahigh mobility in the topological Weyl semimetal candidate NbP , *Nat. Phys.* 11 (2015) 645–649.
- [17] R. Mondal, S. Sasmal, R. Kulkarni, A. Maurya, A. Nakamura, D. Aoki, H. Harima, A. Thamizhavel, Extremely large magnetoresistance, anisotropic Hall effect, and Fermi surface topology in single-crystalline WSi_2 , *Phys. Rev. B* 102 (2020) 115158.
- [18] Y. Zhang, Z. Li, K.-W. Chen, L. Li, C. Uher, Extremely large magnetoresistance and quantum oscillations in semimetal $\text{Ni}_3\text{In}_2\text{S}_2$, *Mater. Today Phys.* 40 (2024) 101318.
- [19] N. Morali, R. Batabyal, P. K. Nag, E. Liu, Q. Xu, Y. Sun, B. Yan, C. Felser, N. Avraham, H. Beidenkopf, Fermi-arc diversity on surface terminations of the magnetic Weyl semimetal $\text{Co}_3\text{Sn}_2\text{S}_2$, *Science* 365 (2019) 1286–1291.
- [20] Q. Wang, Y. Xu, R. Lou, Z. Liu, M. Li, Y. Huang, D. Shen, H. Weng, S. Wang, H. Lei, Large intrinsic anomalous Hall effect in half-metallic ferromagnet $\text{Co}_3\text{Sn}_2\text{S}_2$ with magnetic Weyl fermions, *Nat. Commun.* 9 (2018).
- [21] S. Nakatsuji, N. Kiyohara, T. Higo, Large anomalous Hall effect in a non-collinear antiferromagnet at room temperature, *Nature* 527 (2015) 212–215.
- [22] A. K. Nayak, J. E. Fischer, Y. Sun, B. Yan, J. Karel, A. C. Komarek, C. Shekhar, N. Kumar, W. Schnelle, J. Kübler, et al., Large anomalous

- Hall effect driven by a nonvanishing Berry curvature in the noncollinear antiferromagnet Mn_3Ge , *Sci. Adv.* 2 (2016) e1501870.
- [23] J. Kübler, C. Felser, Weyl fermions in antiferromagnetic Mn_3Sn and Mn_2Ge , *EPL (Europhysics Letters)* 120 (2018) 47002.
- [24] A. Low, S. Ghosh, S. Changdar, S. Routh, S. Purwar, S. Thirupathiah, Tuning of topological properties in the strongly correlated antiferromagnet Mn_3Sn via Fe doping, *Phys. Rev. B* 106 (2022) 144429.
- [25] S. Changdar, S. Ghosh, A. Bose, I. Kar, A. Low, P. L. Fèvre, F. Bertran, A. Narayan, S. Thirupathiah, Weak electronic correlations observed in magnetic Weyl Semimetal Mn_3Ge , *J. Phys. Condens. Matter* 36 (2023) 125502.
- [26] S. Ghosh, A. Low, S. Ghorai, K. Mandal, S. Thirupathiah, Tuning of electrical, magnetic, and topological properties of magnetic Weyl semimetal Mn_{3+x}Ge by Fe doping, *J. Phys. Condens. Matter* 35 (2023) 485701.
- [27] Y.-X. Jiang, J.-X. Yin, M. M. Denner, N. Shumiya, B. R. Ortiz, G. Xu, Z. Guguchia, J. He, S. Hossain, X. Liu, J. Ruff, L. Kautzsch, S. S. Zhang, G. Chang, I. Belopolski, Q. Zhang, T. A. Cochran, D. Multer, M. Litskevich, Z.-J. Cheng, X. P. Yang, Z. Wang, R. Thomale, T. Neupert, S. D. Wilson, M. Z. Hasan, Unconventional chiral charge order in kagome superconductor KV_3Sb_5 , *Nat. Mater.* 20 (2021) 1353–1357.
- [28] Y. Hu, X. Wu, B. R. Ortiz, S. Ju, X. Han, J. Z. Ma, N. C. Plumb, M. Radovic, R. Thomale, S. D. Wilson, A. P. Schnyder, M. Shi, Rich nature of Van Hove singularities in Kagome superconductor CsV_3Sb_5 , *Nat. Commun.* 13 (2022).
- [29] W. Ma, X. Xu, J.-X. Yin, H. Yang, H. Zhou, Z.-J. Cheng, Y. Huang, Z. Qu, F. Wang, M. Z. Hasan, S. Jia, Rare Earth Engineering in RMn_6Sn_6 ($R = \text{Gd-Tm, Lu}$) Topological Kagome Magnets, *Phys. Rev. Lett.* 126 (2021) 246602.
- [30] G. Dhakal, F. Cheenicode Kabeer, A. K. Pathak, F. Kabir, N. Poudel, R. Filippone, J. Casey, A. Pradhan Sakhya, S. Regmi, C. Sims, K. Dimitri, P. Manfrinetti, K. Gofryk, P. M. Oppeneer, M. Neupane, Anisotropically large anomalous and topological Hall effect in a kagome magnet, *Phys. Rev. B* 104 (2021) L161115.
- [31] L. Gao, S. Shen, Q. Wang, W. Shi, Y. Zhao, C. Li, W. Cao, C. Pei, J.-Y. Ge, G. Li, J. Li, Y. Chen, S. Yan, Y. Qi, Anomalous Hall effect in ferrimagnetic metal RMn_6Sn_6 ($R = \text{Tb, Dy, Ho}$) with clean Mn kagome lattice, *Appl. Phys. Lett.* 119 (2021).
- [32] H. Zhou, M. Shi, Y. Huang, W. Ma, X. Xu, J. Wang, S. Jia, Metamagnetic transition and anomalous Hall effect in Mn-based kagomé magnets RMn_6Ge_6 ($R = \text{Tb-Lu}$), *Phys. Rev. Mater.* 7 (2023) 024404.
- [33] C. Q. Xu, T. W. Heitmann, H. Zhang, X. Xu, X. Ke, Magnetic phase transition, magnetoresistance, and anomalous Hall effect in Ga-substituted YMn_6Sn_6 with a ferromagnetic kagome lattice, *Phys. Rev. B* 104 (2021) 024413.
- [34] F. Kabir, R. Filippone, G. Dhakal, Y. Lee, N. Poudel, J. Casey, A. P. Sakhya, S. Regmi, R. Smith, P. Manfrinetti, L. Ke, K. Gofryk, M. Neupane, A. K. Pathak, Unusual magnetic and transport properties in homn_6sn_6 kagome magnet, *Phys. Rev. Mater.* 6 (2022) 064404.
- [35] C. Liu, H. Zhang, Z. Li, Y. Yan, Y. Zhang, Z. Hou, X. Fu, Nontrivial spin textures induced remarkable topological Hall effect and extraordinary magnetoresistance in kagome magnet TmMn_6Sn_6 , *Surfaces and Interfaces* 39 (2023) 102866.
- [36] A. Low, T. K. Bhowmik, S. Ghosh, S. Thirupathiah, Anisotropic nonsaturating magnetoresistance observed in HoMn_6Ge_6 : A kagome Dirac semimetal, *Phys. Rev. B* 109 (2024) 195104.
- [37] S. Peng, Y. Han, G. Pokharel, J. Shen, Z. Li, M. Hashimoto, D. Lu, B. R. Ortiz, Y. Luo, H. Li, M. Guo, B. Wang, S. Cui, Z. Sun, Z. Qiao, S. D. Wilson, J. He, Realizing Kagome Band Structure in Two-Dimensional Kagome Surface States of RV_6Sn_6 ($R = \text{Gd, Ho}$), *Phys. Rev. Lett.* 127 (2021) 266401.
- [38] X. Zhang, Z. Liu, Q. Cui, Q. Guo, N. Wang, L. Shi, H. Zhang, W. Wang, X. Dong, J. Sun, Z. Dun, J. Cheng, Electronic and magnetic properties of intermetallic kagome magnets RV_6Sn_6 ($R = \text{Tb-Tm}$), *Phys. Rev. Mater.* 6 (2022) 105001.
- [39] J. Lee, E. Mun, Anisotropic magnetic property of single crystals RV_6Sn_6 ($R = \text{Y, Gd-Tm, Lu}$), *Phys. Rev. Mater.* 6 (2022) 083401.
- [40] H. W. S. Arachchige, W. R. Meier, M. Marshall, T. Matsuoka, R. Xue, M. A. McGuire, R. P. Hermann, H. Cao, D. Mandrus, Charge Density Wave in Kagome Lattice Intermetallic ScV_6Sn_6 , *Phys. Rev. Lett.* 129 (2022) 216402.
- [41] Y. Liu, M. Lyu, J. Liu, S. Zhang, J. Yang, Z. Du, B. Wang, H. Wei, E. Liu, Structural Determination, Unstable Antiferromagnetism and Transport Properties of Fe-Kagome $\text{Y}_{0.5}\text{Fe}_3\text{Sn}_3$ Single Crystals, *Chinese Phys. Lett.* 40 (2023) 047102.
- [42] P. Giannozzi, S. Baroni, N. Bonini, M. Calandra, R. Car, C. Cavazzoni, D. Ceresoli, G. L. Chiarotti, M. Cococcioni, I. Dabo, A. D. Corso, S. De Gironcoli, S. Fabris, G. Fratesi, R. Gebauer, U. Gerstmann, C. Gougoussis, A. Kokalj, M. Lazzeri, L. Martin-Samos, N. Marzari, F. Mauri, R. Mazzarello, S. Paolini, A. Pasquarello, L. Paulatto, C. Sbraccia, S. Scandolo, G. Sclauzero, A. P. Seitsonen, A. Smogunov, P. Umari, R. M. Wentzcovitch, QUANTUM ESPRESSO: a modular and open-source software project for quantum simulations of materials, *J. Phys. Condens. Matter* 21 (2009) 395502.
- [43] J. P. Perdew, K. Burke, M. Ernzerhof, Generalized Gradient Approximation Made Simple [Phys. Rev. Lett. 77, 3865 (1996)], *Phys. Rev. Lett.* 78 (1997) 1396–1396.
- [44] X.-Y. Zeng, H. Wang, X.-Y. Wang, J.-F. Lin, J. Gong, X.-P. Ma, K. Han, Y.-T. Wang, Z.-Y. Dai, T.-L. Xia, Magnetic and magnetotransport properties in the vanadium-based kagome metals DyV_6Sn_6 and HoV_6Sn_6 , *Phys. Rev. B* 109 (2024) 104412.
- [45] T. Kurumaji, M. Gen, S. Kitou, T.-h. Arima, Metamagnetism and anomalous magnetotransport properties in rare-earth-based polar semimetals RAuGe ($R = \text{Dy, Ho, and Gd}$), *Phys. Rev. B* 110 (2024) 064409.
- [46] J. M. Cadogan, D. H. Ryan, Independent magnetic ordering of the rare-earth (R) and Fe sublattices in the RFe_6Ge_6 and RFe_6Sn_6 series, *J. Alloy. Compd.* 326 (2001) 166–173.
- [47] J. M. Cadogan, Suharyana, D. H. Ryan, O. Može, W. Kockelmann, Neutron diffraction and Mossbauer study of the magnetic structure of HoFe_6Sn_6 , *IEEE Transactions on Magnetics* 37 (2001) 2606–2608.
- [48] J. M. Cadogan, O. Može, D. H. Ryan, Suharyana, M. Hofmann, Magnetic ordering in DyFe_6Sn_6 , *Physica B* 385–386 (2006) 317–319.
- [49] S. Lv, H. Guo, Q. Qi, Y. Li, G. Hu, Q. Zheng, R. Wang, N. Si, K. Zhu, Z. Zhao, Y. Han, W. Yu, G. Xian, L. Huang, L. Bao, X. Lin, J. Pan, S. Du, J. He, H. Yang, H. Gao, Field-Induced Butterfly-Like anisotropic magnetoresistance in a Kagome semimetal $\text{Co}_3\text{In}_2\text{S}_2$, *Adv. Funct. Mater.* (2024).
- [50] R. Singha, A. Pariari, B. Satpati, P. Mandal, Magnetotransport properties and evidence of a topological insulating state in LaSbTe , *Phys. Rev. B* 96 (2017) 245138.
- [51] A. Narayanan, M. D. Watson, S. F. Blake, N. Bruyant, L. Drigo, Y. L. Chen, D. Prabhakaran, B. Yan, C. Felser, T. Kong, P. C. Canfield, A. I. Coldea, Linear Magnetoresistance Caused by Mobility Fluctuations in n -Doped Cd_3As_2 , *Phys. Rev. Lett.* 114 (2015) 117201.
- [52] W. L. Zhu, Y. Cao, P. J. Guo, X. Li, Y. J. Chen, L. J. Zhu, J. B. He, Y. F. Huang, Q. X. Dong, Y. Y. Wang, R. Q. Zhai, Y. B. Ou, G. Q. Zhu, H. Y. Lu, G. Li, G. F. Chen, M. H. Pan, Linear magnetoresistance induced by mobility fluctuations in iodine-intercalated tungsten ditelluride, *Phys. Rev. B* 105 (2022) 125116.
- [53] C. Jin, P. Li, W. B. Mi, H. L. Bai, Magnetocrystalline anisotropy-dependent six-fold symmetric anisotropic magnetoresistance in epitaxial $\text{Co}_x\text{Fe}_{3-x}\text{O}_4$ films, *Europhys. Lett.* 100 (2012) 27006.
- [54] Y. Miao, D. Yang, L. Jia, X. Li, S. Yang, C. Gao, D. Xue, Magnetocrystalline anisotropy correlated negative anisotropic magnetoresistance in epitaxial $\text{Fe}_{30}\text{Co}_{70}$ thin films, *Appl. Phys. Lett.* 118 (2021).
- [55] J. Zhang, X. Chen, M. Wang, Q. Zhang, W. Shi, X. Zhan, M. Zhao, Z. Li, J. Zheng, H. Zhang, F. Han, H. Yang, T. Zhu, B. Liu, F. Hu, B. Shen, Y. Chen, Y. Zhang, Y. Chen, W. Zhao, J. Sun, Proximity-Induced Fully Ferromagnetic Order with Eightfold Magnetic Anisotropy in Heavy Transition Metal Oxide CaRuO_3 , *Adv. Funct. Mater.* 33 (2023).

- [56] R. Ramos, S. K. Arora, I. V. Shvets, Anomalous anisotropic magnetoresistance in epitaxial Fe_3O_4 thin films on $\text{MgO}(001)$, *Phys. Rev. B* 78 (2008) 214402.
- [57] P. Li, E. Y. Jiang, H. L. Bai, Fourfold symmetric anisotropic magnetoresistance based on magnetocrystalline anisotropy and antiphase boundaries in reactive sputtered epitaxial Fe_3O_4 films, *Appl. Phys. Lett.* 96 (2010).
- [58] P. Li, C. Jin, E. Y. Jiang, H. L. Bai, Origin of the twofold and fourfold symmetric anisotropic magnetoresistance in epitaxial Fe_3O_4 films, *J Appl Phys* 108 (2010).
- [59] Z. Li, W. Mi, X. Wang, X. Zhang, Interfacial Exchange Coupling Induced Anomalous Anisotropic Magnetoresistance in Epitaxial $\text{Fe}_4\text{N}/\text{CoN}$ Bilayers, *ACS Appl. Mater. Interfaces* 7 (2015) 3840. PMID: 25643137.
- [60] Y. Dai, Y. W. Zhao, L. Ma, M. Tang, X. P. Qiu, Y. Liu, Z. Yuan, S. M. Zhou, Fourfold Anisotropic Magnetoresistance of Ll_0 FePt Due to Relaxation Time Anisotropy, *Phys. Rev. Lett.* 128 (2022) 247202.
- [61] N. Zhou, Y. Sun, C. Q. Xu, C. Y. Xi, Z. S. Wang, B. Li, J. J. Feng, L. Zhang, X. Z. Xing, Y. F. Zhang, Y. Q. Pan, Y. Meng, X. L. Yi, L. Pi, X. Xu, Z. Shi, Quantum oscillations and anomalous angle-dependent magnetoresistance in the topological candidate Ag_3Sn , *Phys. Rev. B* 101 (2020) 245102.
- [62] C. Hu, J. Zhu, G. Chen, J. Li, Y. Wu, Direct comparison of anisotropic magnetoresistance and planar Hall effect in epitaxial Fe_3O_4 thin films, *Phys. Lett. A* 376 (2012) 3317–3321.
- [63] J. Chen, H. Li, T. Guo, P. Chen, D. Zheng, G. Yu, Y.-C. Lau, X. Xi, W. Wang, Anomalous anisotropic magnetoresistance in the topological semimetal HoPtBi , *NPG Asia Mater.* 15 (2023).
- [64] Z. Zhu, B. Fauqué, K. Behnia, Y. Fuseya, Magnetoresistance and valley degree of freedom in bulk bismuth, *J. Phys. Condens. Matter* 30 (2018) 313001.
- [65] J. Wang, H. Yang, L. Ding, W. You, C. Xi, J. Cheng, Z. Shi, C. Cao, Y. Luo, Z. Zhu, J. Dai, M. Tian, Y. Li, Angle-dependent magnetoresistance and its implications for Lifshitz transition in W_2As_3 , *npj Quantum Materials* 4 (2019).
- [66] S. Zhang, Q. Wu, Y. Liu, O. V. Yazyev, Magnetoresistance from Fermi surface topology, *Phys. Rev. B* 99 (2019) 035142.
- [67] A. Weiland, L. J. Eddy, G. T. McCandless, H. Hodovanets, J. Paglione, J. Y. Chan, Refine intervention: Characterizing disordered $\text{Yb}_{0.5}\text{Co}_3\text{Ge}_3$, *Cryst. Growth Des.* 20 (2020) 6715–6721.
- [68] X. Huang, Z. Cui, C. Huang, M. Huo, H. Liu, J. Li, F. Liang, L. Chen, H. Sun, B. Shen, Y. Zhang, M. Wang, Anisotropic magnetism and electronic properties of the kagome metal SmV_6Sn_6 , *Phys. Rev. Mater.* 7 (2023) 054403.
- [69] K. Guo, J. Ye, S. Guan, S. Jia, Triangular Kondo lattice in YbV_6Sn_6 and its quantum critical behavior in a magnetic field, *Phys. Rev. B* 107 (2023) 205151.
- [70] X. Xu, J. Yin, Z. Qu, S. Jia, Quantum interactions in topological R166 kagome magnet, *Rep. Prog. Phys.* 86 (2023) 114502.
- [71] G. Zheng, J. Lu, X. Zhu, W. Ning, Y. Han, H. Zhang, J. Zhang, C. Xi, J. Yang, H. Du, K. Yang, Y. Zhang, M. Tian, Transport evidence for the three-dimensional Dirac semimetal phase in ZrTe_5 , *Phys. Rev. B* 93 (2016) 115414.
- [72] Q.-H. Yu, Y.-Y. Wang, R. Lou, P.-J. Guo, S. Xu, K. Liu, S. Wang, T.-L. Xia, Magnetoresistance and Shubnikov-de Haas oscillation in YSb , *EPL (Europhysics Letters)* 119 (2017) 17002.
- [73] Q. Wang, P.-J. Guo, S. Sun, C. Li, K. Liu, Z.-Y. Lu, H. Lei, Extremely large magnetoresistance and high-density Dirac-like fermions in ZrB_2 , *Phys Rev B* 97 (2018) 205105.
- [74] Y.-Y. Lv, X. Li, J. Zhang, B. Pang, S.-S. Chen, L. Cao, B.-B. Zhang, D. Lin, Y. B. Chen, S.-H. Yao, J. Zhou, S.-T. Zhang, M.-H. Lu, M. Tian, Y.-F. Chen, Mobility-controlled extremely large magnetoresistance in perfect electron-hole compensated $\alpha\text{-WP}_2$ crystals, *Phys. Rev. B* 97 (2018) 245151.

6. Supplementary Information

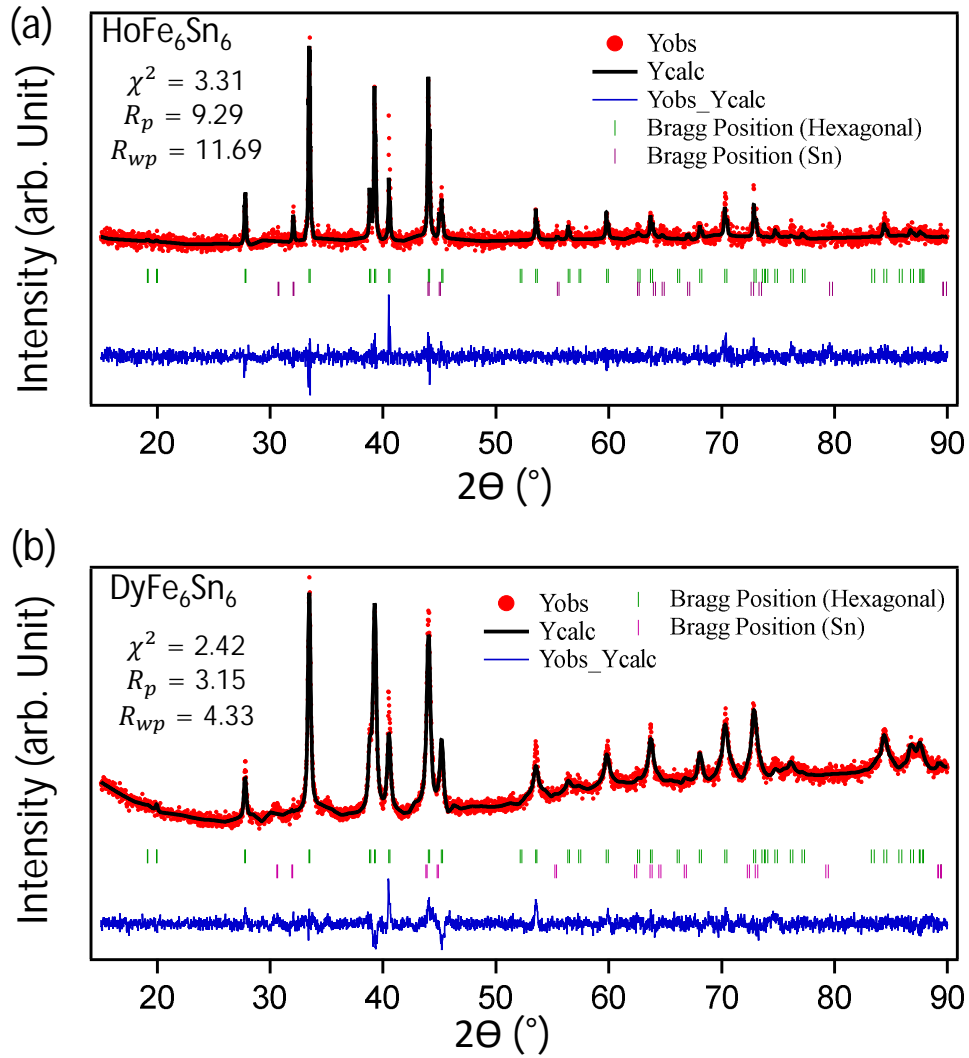


Fig. S 1: (a) Powder X-ray diffraction pattern of the crushed single crystals of HoFe_6Sn_6 (a) and DyFe_6Sn_6 (b), overlapped with Rietveld refinement. Since large number of single crystals were crushed for powder XRD, some amount of Sn flux also got mixed with the powders, resulting in as impurity peaks.

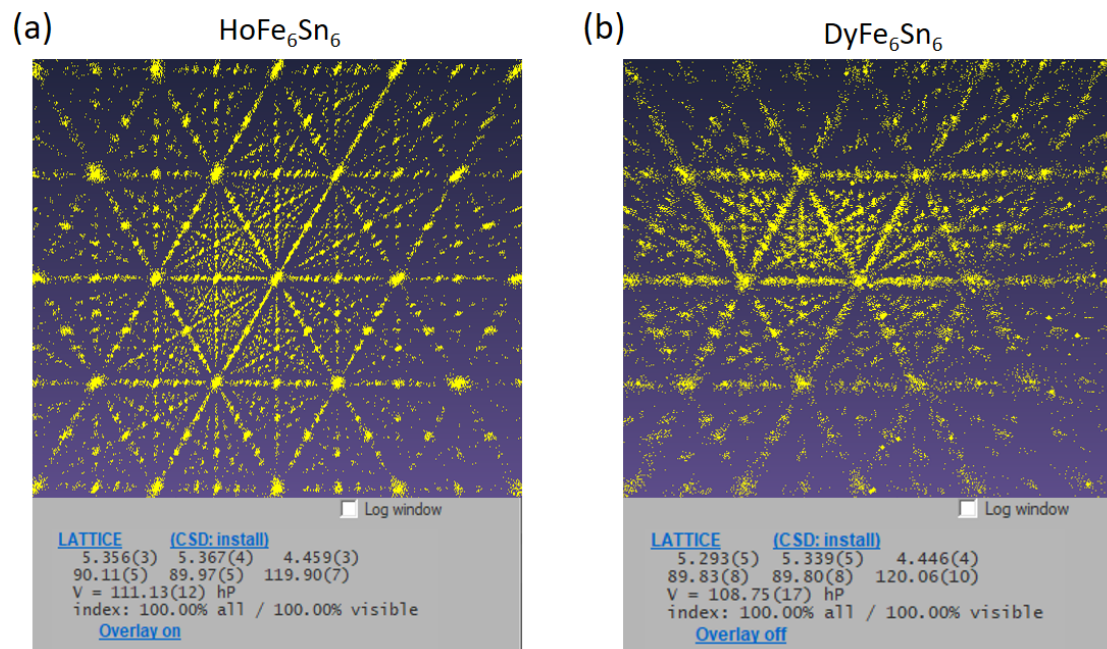


Fig. S 2: Gnomonic projection of single crystal XRD (SCXRD) pattern using the Ewald's explorer-reciprocal space option in CrysAlispro software of (a) HoFe_6Sn_6 and (b) DyFe_6Sn_6 . The SCXRD data show perfect hexagonal pattern and the obtained lattice parameters are mentioned in the bottom of respective panels, confirming the Hexagonal crystal structure of the studied systems.

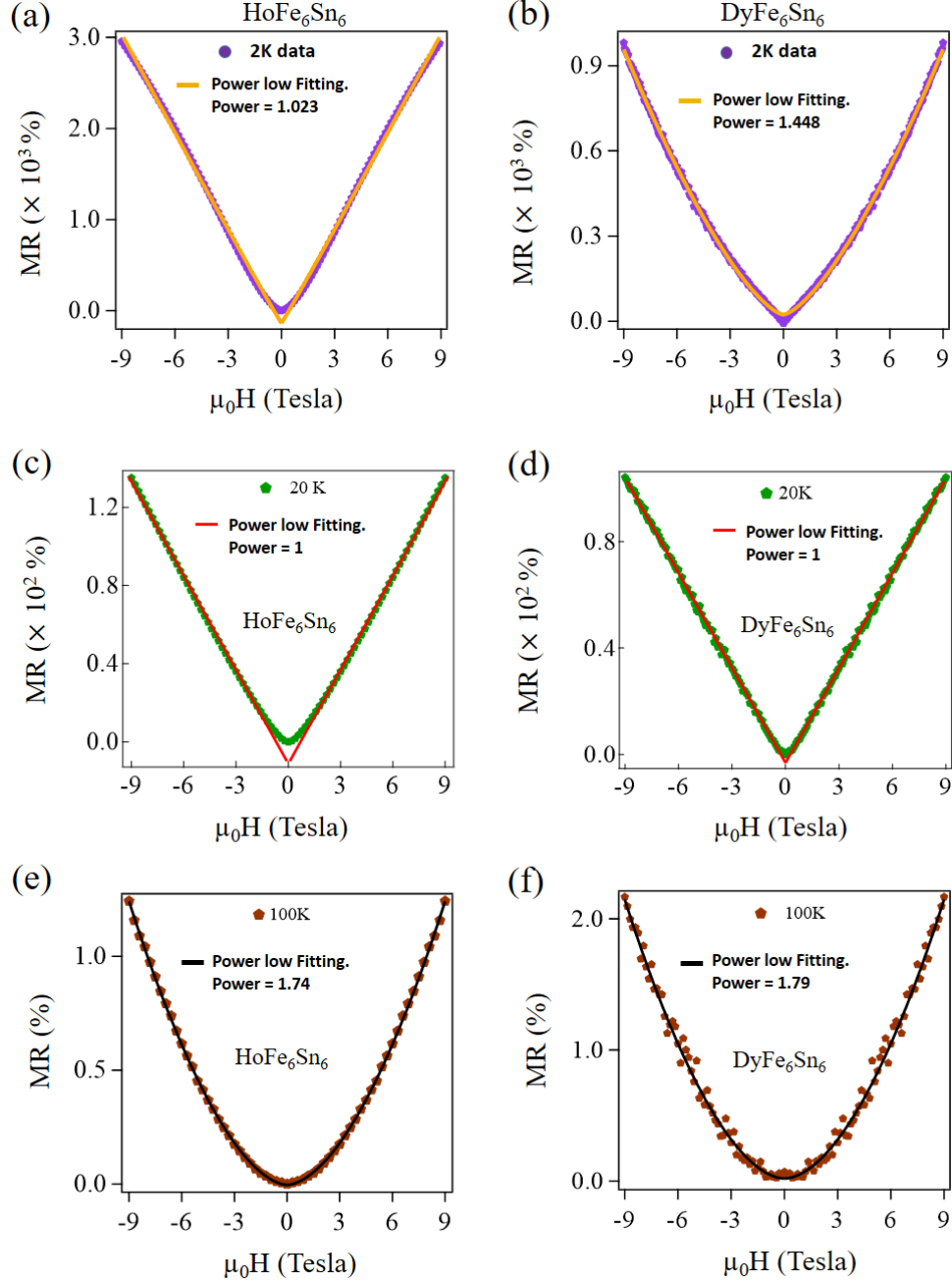


Fig. S 3: (a)-(f) Field-dependent magnetoresistance (MR) fitted with power law (MR $\propto B^m$) at different temperatures for HoFe_6Sn_6 and DyFe_6Sn_6 .

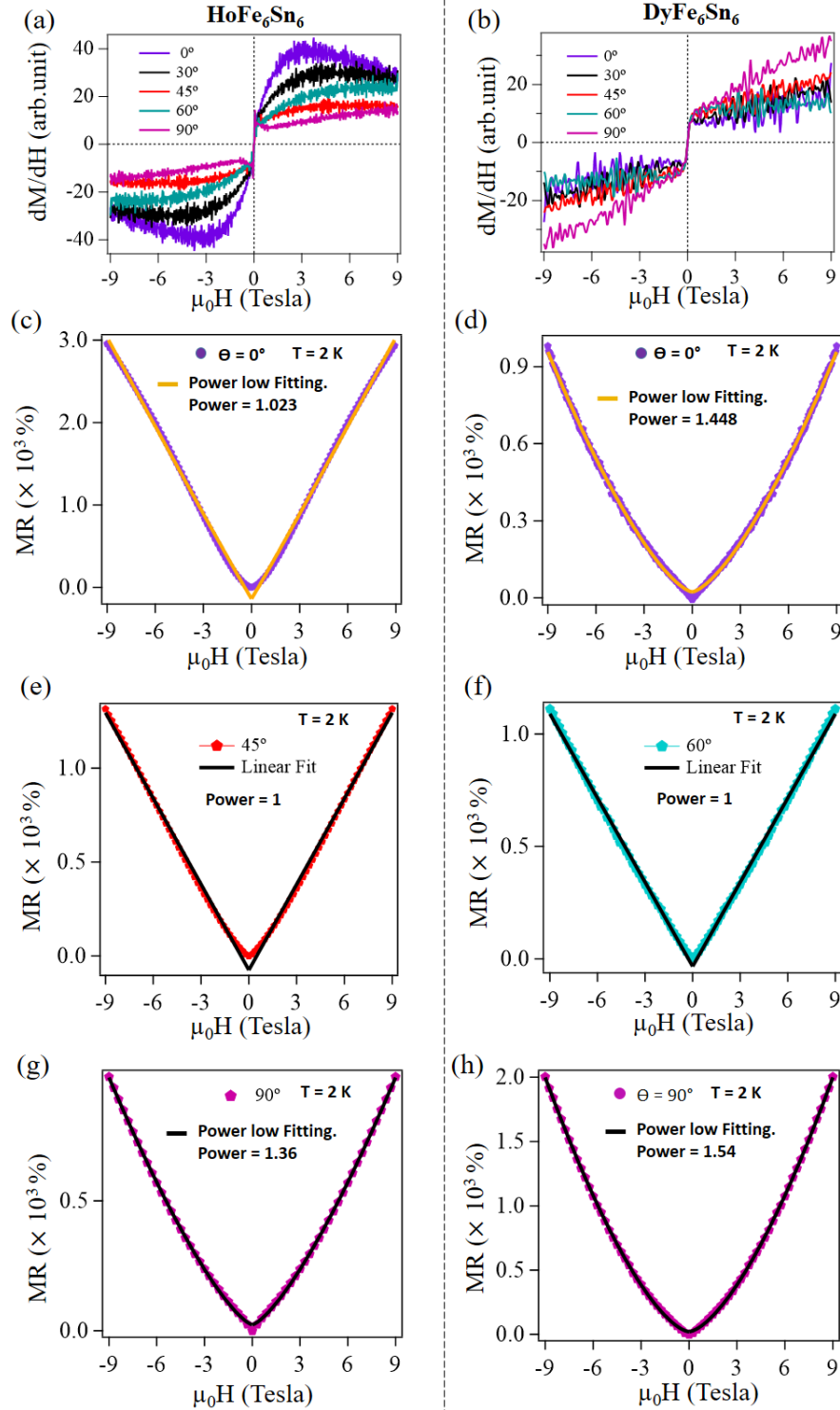


Fig. S 4: First derivative of MR with respect to field at different field angles measured at 2 K for (a) HoFe_6Sn_6 and (b) DyFe_6Sn_6 . (c), (e), (g), and (d), (f), (h) are field-dependent MR fitted with power law ($\text{MR} \propto B^m$) at different field angles measured at 2 K for HoFe_6Sn_6 and DyFe_6Sn_6 respectively.

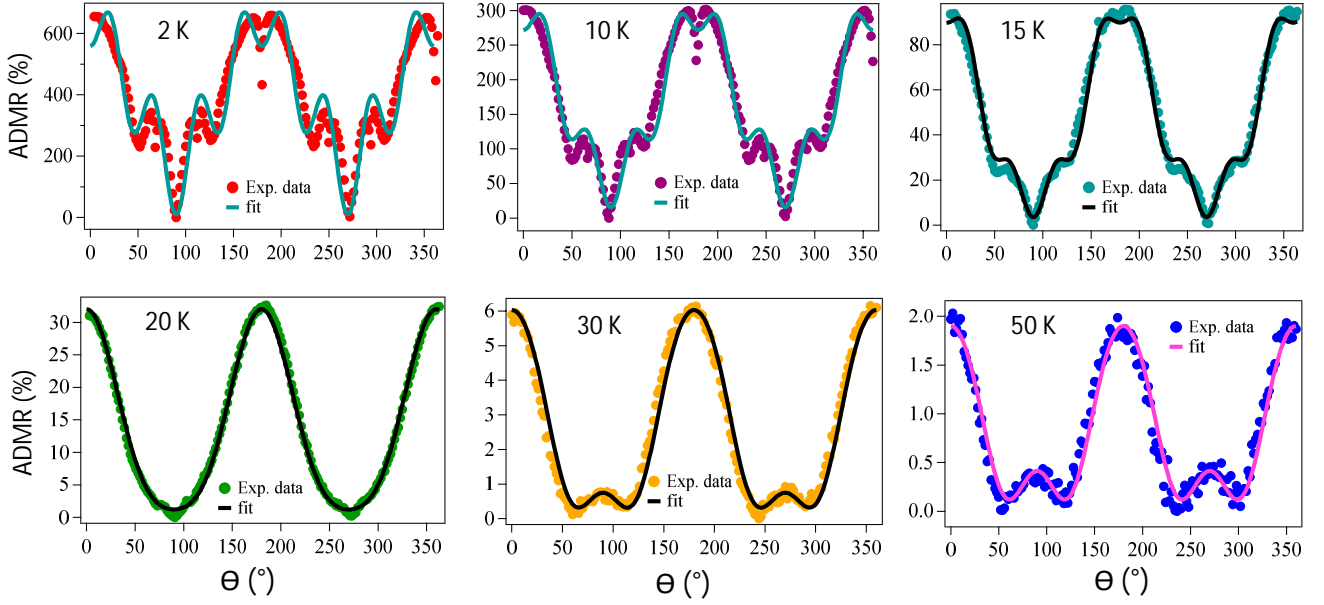


Fig. S 5: Angle-dependent magnetoresistance (ADMR) measured at various temperatures under the magnetic field of 9 T for HoFe_6Sn_6 . The solid lines show fits of ADMR.

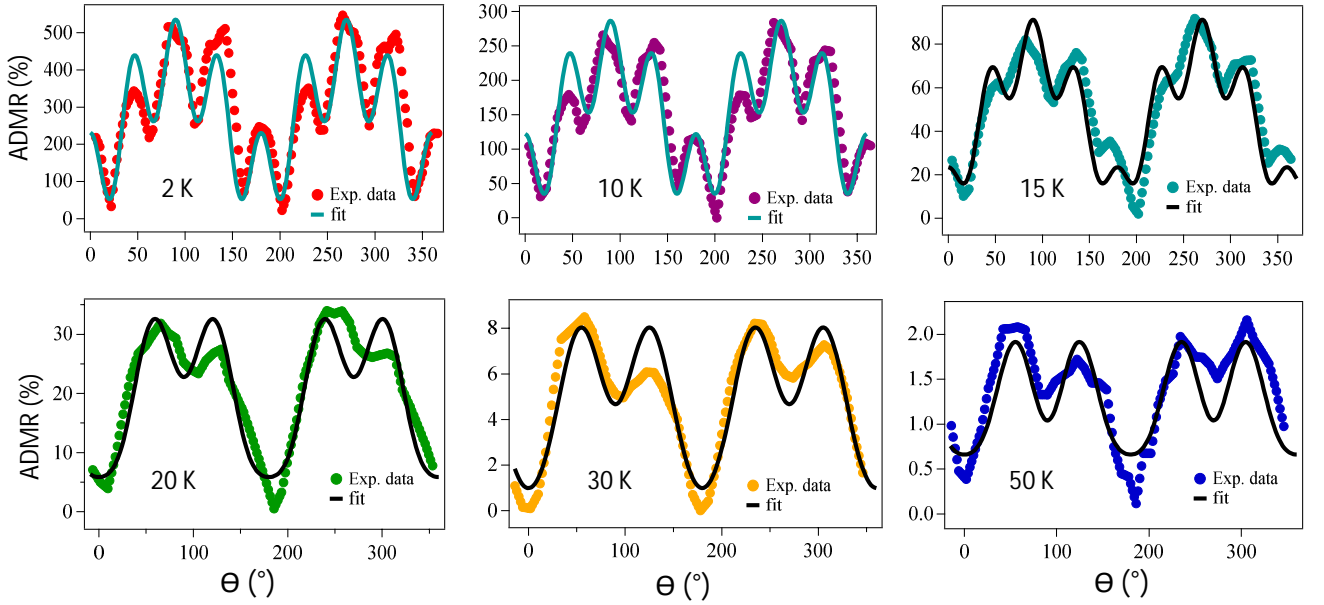


Fig. S 6: Angle-dependent magnetoresistance (ADMR) measured at various temperatures under the magnetic field of 9 T for DyFe_6Sn_6 . The solid lines show fits of ADMR.

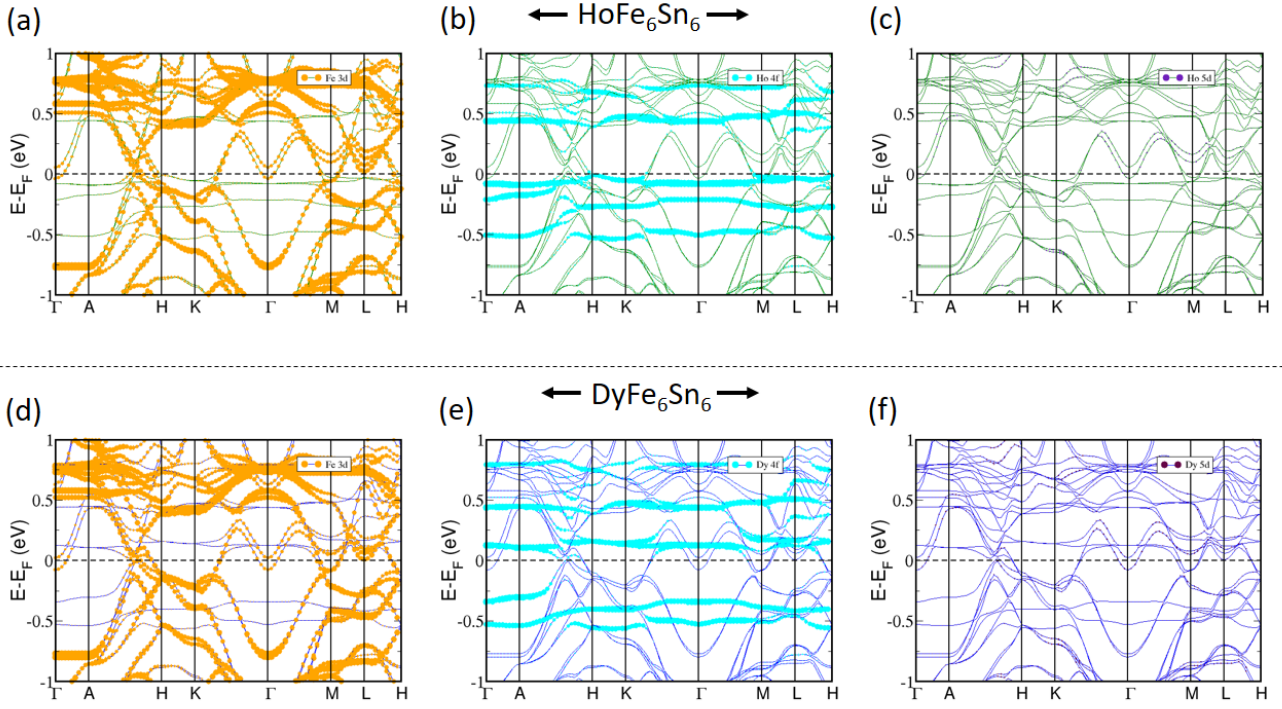


Fig. S 7: Band structure of HoFe_6Sn_6 for (a) Fe 3d, (b) Ho 4f, and (c) Ho 5d orbitals. Band structure of DyFe_6Sn_6 for (d) Fe 3d, (e) Dy 4f, and (f) Dy 5d orbitals.

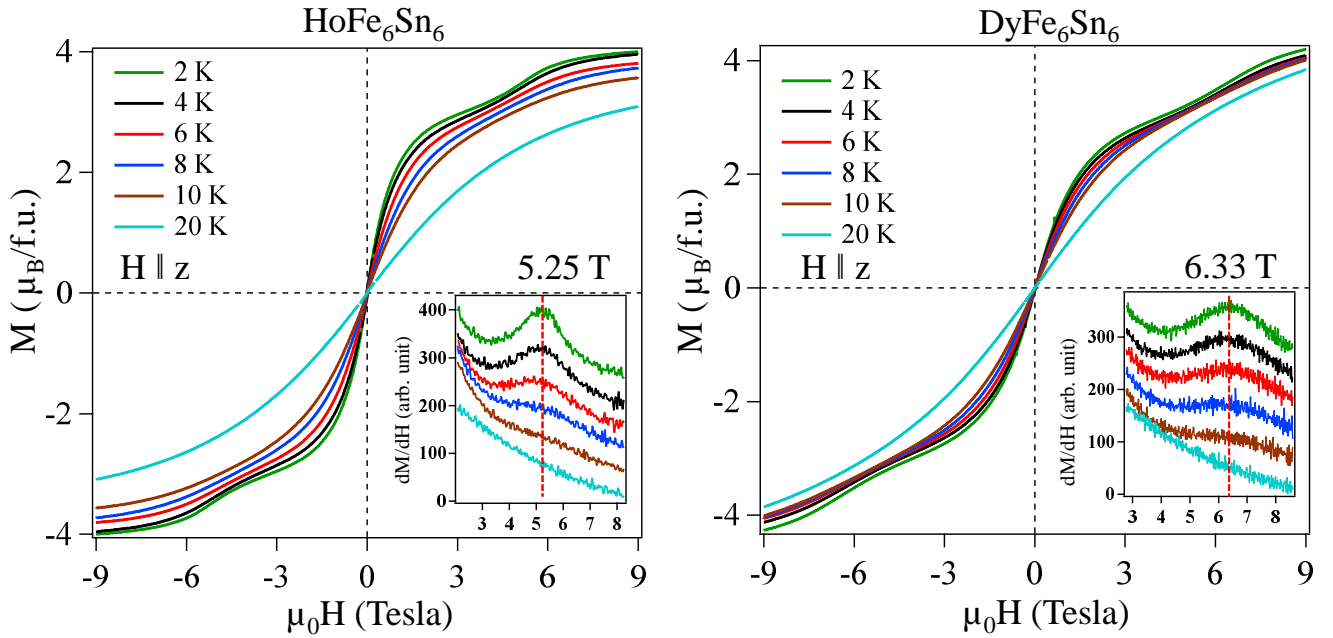


Fig. S 8: Isothermal magnetization $M(H)$ data taken at various temperatures for HoFe_6Sn_6 (a) and DyFe_6Sn_6 (b). First derivatives (dM/dH) are shown in the insets. Vertical dashed line in the insets suggest the field position of metamagnetic state.